

POLITECNICO DI TORINO

Corso di Laurea in Ingegneria Meccanica e Aerospaziale

Tesi di Laurea Magistrale

**Analytical methods for fluid
driven crack-propagation with
application to geothermal case
study**



Relatore

prof. Stefano BERRONE

Candidato

Francesca RISI

Supervisore aziendale

Helmholtz Centre for Environmental Research-UFZ

dott. Francesco PARISIO

A.A. 2017 – 2018

Summary

This thesis analyze the problem of a penny-shaped hydraulic fracture; the hydraulic fracturing process consists of tensile cracks driven by high-pressure fluid injection in a permeable medium. The Newtonian incompressible fluid is injected with a constant flow rate in the rock where there are pre-existing compressive stresses.

The problem is defined by a physico-mathematical model, that allows to describe the propagation regimes using different scalings. In every propagation time, the system is described by exact equations, but, during the evolution from one vertex solution to another, it is used a numerical algorithm. Dontsov demonstrated the validity of his approximate solution, so, using it, it is possible to obtain as a result all that is necessary to describe the fracture design as a function of the time.

The semi-analytical solution of fluid-driven fracture propagation has been applied on two geothermal case study: EAC1 and EAC2 are two wellbore site in a high-temperature geothermal reservoir, the Acoculco caldera, in Mexico.

The simulation focuses the attention on the rock and fluid's parameters and how they influence the dimension of the fracture radius. Indeed, the system parameters change with the depth, as the temperature changes, so it is possible to deduce what is the optimal depth to be excavated. This result is obtained not only valuing where the biggest fracture radius is in a given instant time, but studying the system efficiency trend over the depth and over the time, as well.

The results of the two wellbores are different: concerning the EAC2 well, the bigger fracture radius corresponds to the higher efficiency at one instant time; instead, in the EAC1 well the bigger fracture radius is not where the efficiency is higher and it depends on the evolution of the system parameters defined as a function of the depth. From the simulation it can be confirmed that the best choice is not to dig where the fracture radius is bigger, but it is necessary to evaluate efficiency at the same depth, as well.

List of Figures

1.1	Schematic of an hydraulic fracturing treatment.	2
2.1	Penny-shaped hydraulic fracture.	6
3.1	Crack opening and net pressure in the viscosity dominated regime.	11
3.2	Crack opening in the toughness dominated regime.	12
3.3	Crack opening and net pressure in the viscosity–leak-off dominated regime.	13
3.4	Crack opening in the toughness–leak-off dominated regime.	14
3.5	Rectangular phase diagram $MK\tilde{K}\tilde{M}$	16
3.6	Crack opening, net pressure and fracture radius over the dimensionless time. Π is calculated in $\rho = 0.5$ and Ω is calculated at the first node.	18
3.7	Crack opening, net pressure and fracture radius over the dimensionless time. Π is calculated in $\rho = 0.5$ and Ω is calculated at the first node.	19
3.8	Design fracture after 1 second.	20
4.1	Variation of the approximate solution versus dimensionless time and the leak-off parameter.	24
4.2	Comparing approximate solution with M - and K -vertex solution of the crack opening, net pressure and fracture radius over the dimensionless time. Π is calculated in $\rho = 0.5$ and Ω is calculated at the first node.	25
4.3	Comparing approximate solution with M - and \tilde{M} -vertex solution of the crack opening, net pressure and fracture radius over the dimensionless time. Π is calculated in $\rho = 0.5$ and Ω is calculated at the first node.	26
4.4	Interpolation of the error’s results in logarithmic scale between numerical and approximate solution.	27

4.5	Comparing approximate solutions in different instant times, with vertex solutions of the crack opening over the dimensionless radius. Width and pressure are normalized by the M -vertex solution calculated in $\rho = 0$ and $\rho = 0.5$, respectively.	28
4.6	Comparing approximate solutions in different instant times, with vertex solutions of the crack opening over the dimensionless radius. Width and pressure are normalized by the M -vertex solution calculated in $\rho = 0$ and $\rho = 0.5$, respectively.	29
4.7	Efficiency over the dimensionless time in MK and in $M\tilde{M}$ edge.	30
4.8	Fracture design comparing numerical and approximate solution after $t = 1s$	30
5.1	Location of the Acoculco geothermal zone [13].	34
5.2	Compressibility, viscosity and toughness trend as a function of the depth for both wellbore EAC1 and EAC2.	39
5.3	Temperature trend as a function of the depth for both wellbore EAC1 and EAC2.	40
5.4	The main cross-section for EAC1 and EAC2 wellbores.	40
5.5	Carter's leak-off trend as a function of the depth for both wellbore EAC1 and EAC2.	41
5.6	\hat{K} trend as a function of the temperature.	42
5.7	Fracture radius trend as a function of the depth for both wellbore EAC1 and EAC2 at time $t = 7200s$	43
5.8	Efficiency trend as a function of the depth for both wellbore EAC1 and EAC2 at time $t = 7200s$	44
5.9	Fracture radius trend for both wellbore EAC1 and EAC2 at different instant times and different flow rate. Blue line - $Q_0 = 0.08m^3/s$ at $t = 7200s$, red line - $Q_0 = 0.04m^3/s$ at $t = 14400s$, yellow line - $Q_0 = 0.16m^3/s$ at $t = 3600s$	45
5.10	K_I as a function of the depth in the two different considered cases for both wellbore EAC1 and EAC2.	46
5.11	Fracture radius trend as a function of the depth for both wellbore EAC1 and EAC2 at different time $t = 7200s$	47
5.12	Carter's leak-off coefficient trend for both wellbore EAC1 and EAC2 with different flow rate. Blue line - $Q_0 = 0.08m^3/s$, red line - $Q_0 = 0.04m^3/s$, yellow line - $Q_0 = 0.16m^3/s$	48
5.13	Fracture radius trend for both wellbore EAC1 and EAC2 at different instant times and different flow rate. Blue line - $Q_0 = 0.08m^3/s$ at $t = 7200s$, red line - $Q_0 = 0.04m^3/s$ at $t = 14400s$, yellow line - $Q_0 = 0.16m^3/s$ at $t = 3600s$	49
5.14	Viscosity trend for both wellbore EAC1 and EAC2 at different instant times and different flow rate.	50

6.1	Fracture radius and efficiency trend over the time for both wellbores EAC1 and EAC2.	53
6.2	Efficiency trend over the time for both wellbores EAC1 at 3000 m depth.	54

List of Tables

3.1	Dimensionless times equations.	15
3.2	Evolution parameters equations	15
3.3	Π_{mk} , Ω_{mk} and γ_{mk} depending on τ along MK -edge	17
3.4	$\Pi_{m\tilde{m}}$, $\Omega_{m\tilde{m}}$ and $\gamma_{m\tilde{m}}$ depending on τ along $M\tilde{M}$ -edge	17
4.1	Value of the dimensionless time along each edge.	24
5.1	EAC1 model parameters.	34
5.2	EAC2 model parameters.	35
6.1	Maximum values of the fracture radius and the corresponding depth for both wellbore EAC1 and EAC2.	52
6.2	Efficiency's values at the depths where the fracture radius is maximum for both wellbores EAC1 and EAC2.	52

Contents

List of Figures	II
List of Tables	V
1 Introduction	1
1.1 Preamble	1
1.2 Motivation and background	2
1.3 Objectives and organization	3
2 Theory model	5
2.1 Problem formulation	5
2.2 Governing equations	6
2.3 Boundary and initial conditions	8
2.3.1 Boundary conditions	8
2.3.2 Initial conditions	8
2.4 Conclusions	8
3 Dimensionless problem formulation	9
3.1 Vertex solutions	10
3.1.1 Zero toughness asymptotic solution	10
3.1.2 Large toughness asymptotic solution	11
3.1.3 Zero toughness–leak-off asymptotic solution	12
3.1.4 Large toughness–leak-off asymptotic solution	14
3.2 Time-based scaling	14
3.2.1 Relationships between scalings	16
3.3 Conclusions	17
4 Approximate solution for a penny shaped hydro-fracture	21
4.1 Solution in scaled variables	22
4.2 Numerical algorithm	23
4.3 Time-based scaling	24
4.3.1 Comparison with numerical solution	26

4.4	Conclusions	28
5	Application to geothermal case study	33
5.1	Numerical model	33
5.2	Results	36
5.2.1	Fracture radius	36
5.2.2	Efficiency	36
5.3	Influence of the rock and fluid's parameters on the radius	37
5.3.1	Flow rate	37
5.3.2	Toughness	37
5.3.3	Carter's leak-off	38
5.3.4	Viscosity	38
6	Conclusions	51
A	Carter's leak off	55
	Bibliography	56

Chapter 1

Introduction

1.1 Preamble

Hydraulic fractures are tensile cracks that are driven by high-pressure fluid injection. They propagate in solid media subjected to pre-existing compressive stresses [4]. This technique is mainly used in the petroleum industry to enhance the recovery of oil and gas from underground hydrocarbon reservoirs and in the geothermal industry to enhanced permeability and enable fluid circulation. [16].

The procedure, consists of injecting a viscous fluid into a well under high pressure to initiate and propagate a fracture, as shown in Figure 1.1. Actually hydraulic fracturing involves multiple processes, such us:

- fracture growth,
- fluid flow in the fracture itself and in the rock,
- proppant transport,
- rock deformation.

To be able to design a treatment, it is necessary to predicto the opening and the size of the fracture as well as the pressure of the fracturing fluid, as a function of the properties of the rock and the fluid. The man-made fracture extends into the reservoir rock typically about 50 m to 300 m from the wellbore [11].

Hydraulic fractures can propagate vertically, due to the nature of the in situ stress, or horizontally, under ideal situations [11]. The necessary steps to the hydraulic fracturing process are:

1. a well is drilled into a reservoir rock;
2. a fluid is injected into the well;

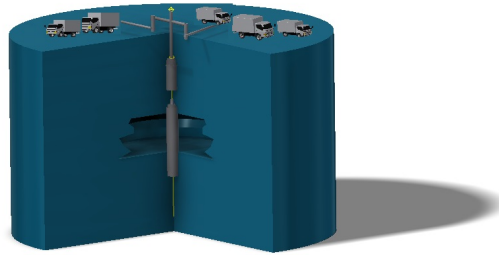


Figure 1.1: Schematic of an hydraulic fracturing treatment.

3. when the fracture is wide enough, due to the pad that reduces the frictional losses in the wellbore, the solid particles are added to the fracturing fluid to increase the fluid viscosity;
4. the injected fluid are removed from the well, while the proppant is left inside the fracture;
5. the resulting low viscosity fluids travel through the fracture to the well and up to the surface;
6. the propped fracture is finally a high-permeability channel for the fluid transportation.

The polymer content of the fracturing fluid is partly intended to impede the loss of fluid. The phenomenon is envisioned as continuous built-up of a thin layer of packed propping agents with chemical additives, *filter cake*, which manifests ever increasing resistance to flow through the fracture face. Indeed, the fluid loss is one of the most important problem in hydraulic fracturing: the rate of fluid infiltration into the rock impact on the success of a fracturing treatment [11].

1.2 Motivation and background

There is a significant number of possible fracture geometry because of the several possible combinations of the parameters involved. The Kristianovich-Geertsma-de Klerk (KGD) radial model and the Perkins-Kern-Nordgren (PKN) model are two examples of idealized models and they are useful to study the process: they are 2D hydraulic fracturing model and the second one is considered and they let it be possible to analyze the influence of the various problem parameters.

The system, defined by integral and non linear differential equations, is very complex. The respective mathematical formulation has been applied on two different case study: the stimulation scenario of EAC1 and EAC2 wells that are located in the Acoculco caldera, which has a diameter of 18 km and lies within an older and wider caldera, the Tulancingo caldera [13].

Knowing the temperature profile and all the process parameters, it has been possible to obtain results about the fracture design. These informations are relevant because they allow to know how system's geometry change when one or some of the parameters change. This means that it was possible to know how the fracture radius change with the increasing of the time and what is the efficiency's trend in each depth.

1.3 Objectives and organization

The main objective of the research is to employ existing analytical solutions of fluid-driven fracture propagation to study the stimulation response in high-temperature geothermal reservoir. Each of the propagation regimes corresponds to the dominance of one of the fluid storage mechanism and one of the energy dissipation mechanism. Indeed regarding the fluid storage mechanism, it can happen that either the fluid stores inside the fracture or leaks into the surrounding medium.

Asymptotic cases has been used to check the accuracy of the numerical solution, that has been applied to study which is the optimal depth to reach drilling.

The structure of the thesis is as follows.

A physico-mathematical model of our problem is formulated in Chapter 2. In Chapter 3, different scalings for the corresponding predominant propagation regimes are discussed. It has been possible to demonstrate that the dimensionless time and η parameters are the only terms which dimensionless form of the governing equations depend on. Chapter 4 presents the approximate solutions and their validation, comparing them with the vertex solutions at different time instants. The application of the numerical algorithm on the two geothermal case study and the results obtained are shown in Chapter 5. Finally the numerical results are discussed with the main conclusions of the research in Chapter 6.

Chapter 2

Theory model

I consider here the theory of fluid driven crack-propagation in porous media as developed in [16]. The theory model considers a penny-shaped hydraulic fracture, where a pressurized incompressible Newtonian fluid propagates in a permeable, linear elastic medium. The fracture propagates quasi-statically and perpendicular to a uniform far-field stress σ_0 , i.e. along the x direction, perpendicularly to the fracture surface; furthermore the fracture growth is governed by mode I of linear elastic fracture mechanics (LEFM), [16].

As seen from Figure 2.1, the radius of the wellbore is negligible compared to the radius of the fracture and it is possible to hypothesize that there is just one single planar hydraulically induced fracture: the one of which study opening $w(r, t)$ and radius $R(t)$ will be studied.

Furthermore the geometry and loading conditions can be assumed to be an ellipse-detailed information on the peculiarities of the shape is not available [1].

2.1 Problem formulation

The parameters needed to characterize the rock, assumed to be linear, elastic and homogeneous, are: Young's modulus, E , Poisson's ratio, ν , fracture toughness, K_{Ic} and leak-off coefficient, C_L .

The fluid with a dynamic viscosity μ is injected at the center of the fracture at constant volumetric rate Q_0 .

Several assumptions are introduced to simplify this problem:

1. the fluid is injected from a point source;
2. the fluid front coincides with the crack front: the lag between the fracture tip

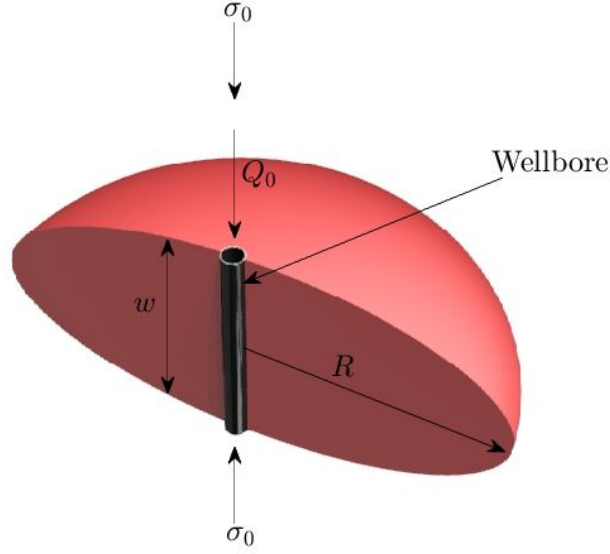


Figure 2.1: Penny-shaped hydraulic fracture.

and the fluid front is very small compared to the fracture radius. This means that the solution does not depend on the far-field stress.

3. the fracture propagates continuously in mobile equilibrium;
4. the fluid flow follows lubrication theory;
5. the effect of gravity is neglected.

The formulation of the problem is based on elasticity and lubrication theories, on fracture propagation criterion from LEFM and on boundary conditions applied at the inlet and at the tip of the fracture.

2.2 Governing equations

The fluid continuity equation:

$$\frac{\partial w}{\partial t} + \frac{1}{r} \frac{\partial}{\partial r} (rq) + \frac{2C_L}{\sqrt{t - t_0(r)}} = Q_0 \delta(r), \quad (2.1)$$

where q is the fluid flow in the radial direction, w is the fracture width, t is the time and $t_0(r)$ is the time instant at which the fracture front was located at point r , that indicates the radial coordinate.

Elasticity equation: the pressure $p(r, t)$ of the fluid inside the fracture is

$$p(r, t) = -\frac{E'}{R} \int_0^1 \mathcal{M}(\rho, s) \frac{\partial w}{\partial s} ds, \quad (2.2)$$

where $\rho = r/R$ is the ratio between the radial coordinate and the fracture radius, $E' = E/(1 - \nu^2)$ is the plane strain modulus and the kernel \mathcal{M} is given by [3]

$$\mathcal{M}(\rho, s) = \frac{1}{2\pi} \begin{cases} \frac{1}{\rho} \mathcal{K}\left(\frac{s^2}{\rho^2}\right) + \frac{\rho}{s^2 - \rho^2} \mathcal{E}\left(\frac{s^2}{\rho^2}\right) & \rho > s \\ \frac{s}{s^2 - \rho^2} \mathcal{E}\left(\frac{\rho^2}{s^2}\right) & \rho \leq s, \end{cases} \quad (2.3)$$

with $\mathcal{K}(\cdot)$ and $\mathcal{E}(\cdot)$ are the complete elliptic integrals of the first and second kind respectively.

Poiseuille Equation: the fluid flow is given by

$$q = -\frac{w^3}{12\mu} \frac{\partial p}{\partial r}. \quad (2.4)$$

Fluid volume balance: all the fluid volume injected in the fracture is equal to the sum of the volume of the crack and the fluid lost into the rock at any time instant

$$\frac{1}{2\pi} \int_0^t Q_0 dt = \int_0^R r w dr + \int_0^t \int_0^{R(\tau)} r \frac{2C_L}{\sqrt{t - t_0(r)}} dr d\tau. \quad (2.5)$$

Fracture propagation criterion: the mode I stress intensity factor K_I is equal to the material toughness K_{Ic} and this is always true thanks to the assumption that it is considered a system with no lag.

For a penny-shaped fracture

$$K_I = \frac{2}{\sqrt{\pi R}} \int_0^R \frac{p(r, t)}{\sqrt{R^2 - r^2}} r dr. \quad (2.6)$$

The fracture opening in the vicinity of the crack tip follows

$$w \simeq \frac{8}{\sqrt{2\pi}} \frac{K_I}{E'} \sqrt{R - r}, \quad 1 - \frac{r}{R} \ll 1. \quad (2.7)$$

Imposing the condition according to which $K_I = K_{Ic}$, the fracture is always propagating and energy is dissipated continuously in the creation of the new fracture surfaces in the solid material [11]. Indeed if the stress intensity factor at the tip is lower than the fracture toughness, the fracture is stable, otherwise the fracture is unstable and starts to propagate [18]. Furthermore, it is necessary to hypothesize that the stress intensity factor at a crack tip does not increase with a crack length.

2.3 Boundary and initial conditions

2.3.1 Boundary conditions

The fracture tip is characterized by zero fracture opening, i.e.

$$w = 0, \quad r = R, \quad (2.8)$$

which amounts to a Neumann boundary condition [14], and no flow

$$q = 0, \quad r = R. \quad (2.9)$$

Combining 2.4 and 2.9 leads to

$$w^3 \frac{\partial p}{\partial r} = 0. \quad (2.10)$$

Since fluid is injected from a punctual source, injection of fluid in the wellbore is idealized as it is from the center of the fracture. The source can be expressed as

$$2\pi \lim_{r \rightarrow 0} r q = Q_0, \quad (2.11)$$

near the source $q \simeq 1/r$ and, combining it with 2.4, it follows that at the source $p \simeq -\ln r$.

2.3.2 Initial conditions

Functions $w(r, t)$, $p(r, t)$ and $R(t)$ can be determined using the set of the equations described in Chapter 2.2, with $0 \leq r \leq R(t)$ and $t \geq t_0$, starting from known values of these quantities at an initial time t_0 .

Considering the assumptions according to which the fluid is injected from a point source and it reaches the tip of the crack, the influence of the initial conditions has vanished for the particular solution [16].

2.4 Conclusions

Governing equations, combined to the boundary conditions, are used to find the equations of the system that describe all the parameter on which the attention will be focused: fluid pressure, fracture radius and wellbore opening.

Indeed the conditions described in Equations 2.8 and 2.9 provide the necessary information to find the solution of the system.

Chapter 3

Dimensionless problem formulation

I report here the solution originally proposed by [16]. For practicality the five parameters that describe the physics of the problem are written as follow[16]

$$\mu' = 12\mu, \quad K' = \frac{8}{\sqrt{2\pi}}K_{Ic}, \quad C' = 2C_L, \quad (3.1)$$

that for simplicity are defined as viscosity, toughness and leak-off coefficients, respectively.

Eight dimensionless evolution parameters, depending monotonically on time t , that can be defined as \mathcal{P} , are used to describe fracture opening (w), net pressure (p) and the crack radius (R) as

$$w(r, t) = \varepsilon(t)L(t)\Omega(\rho, \mathcal{P}(t)), \quad (3.2)$$

$$p(r, t) = \varepsilon(t)E'\Pi(\rho, \mathcal{P}(t)), \quad (3.3)$$

$$R(t) = L(t)\gamma(\mathcal{P}(t)), \quad (3.4)$$

where ε is a small dimensionless number, L is a length scale respectively of the same order of magnitude as the fracture radius R ; $\Omega(\rho, \mathcal{P}(t))$, $\Pi(\rho, \mathcal{P}(t))$ and $\gamma(\mathcal{P}(t))$ are the dimensionless crack opening, net pressure and fracture radius, respectively; explicit forms of the parameters $\varepsilon(t)$, $L(t)$ and \mathcal{P} are summarized in Table 3.2 for different scaling.

Four primary asymptotic regimes of hydraulic fracture propagation can be identified, in which one of the two dissipative mechanism and one of the two fluid storage components vanish [5]:

- storage viscosity M ;
- storage toughness K ;
- leak-off viscosity \tilde{M} ;
- leak-off toughness \tilde{K} .

M and \tilde{M} solutions have negligible toughness; instead in K and \tilde{K} solutions the effect of the fluid viscosity is negligible. \tilde{M} and \tilde{K} have in common the fact that the fluid leaks into the formation; conversely the fluid is stored in the fracture in M and K solutions.

3.1 Vertex solutions

3.1.1 Zero toughness asymptotic solution

Now, M vertex solution is considered, where leak-off and toughness are both negligible. This solution is described by the M vertex scaling where the following expressions apply [16]

$$\Omega_{m0} = \left[\frac{\sqrt{70}}{3} C_1 + \frac{4\sqrt{5}}{9} C_2 (13\rho - 6) \right] (1 - \rho)^{2/3} + B \left[\frac{8}{\pi} (1 - \rho)^{1/2} - \frac{8}{\pi} \rho \arccos \rho \right], \quad (3.5)$$

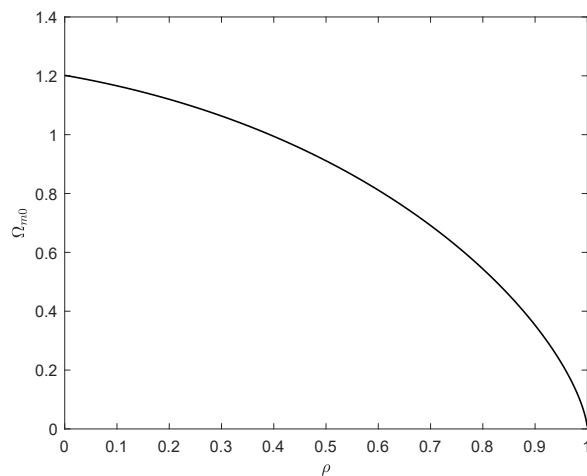
$$\Pi_{m0} = A_1 \left[\omega_1 - \frac{2}{3(1 - \rho)^{1/3}} \right] - B \left(\ln \frac{\rho}{2} + 1 \right), \quad (3.6)$$

$$\gamma_{m0} \simeq 0.6976, \quad (3.7)$$

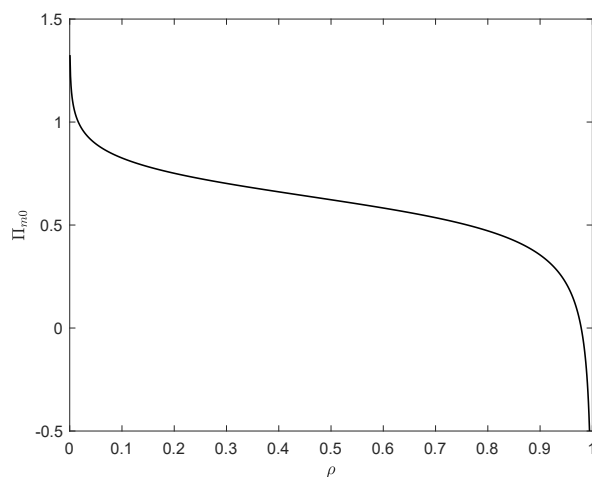
where $A_1 \simeq 0.3581$, $C_1 \simeq 0.6848$, $C_2 \simeq 0.07098$, $B \simeq 0.09269$ and $\omega_1 \simeq 2.479$.

The Figures 3.1a and 3.1b show crack opening, Ω_{m0} , and net pressure, Π_{m0} , in viscosity-dominated regime as a function of the distance from the center of the fracture.

It is possible to notice from Equation 3.6 and looking at the Figure 3.1b that when $\rho \rightarrow 0$, $\Pi_{m0} \rightarrow \infty$ and when $\rho \rightarrow 1$, $\Pi_{m0} \rightarrow -\infty$; that means that, for what concerns pressure, near the wellbore and near the tip, the M solution does not give precise results.



(a)



(b)

Figure 3.1: Crack opening and net pressure in the viscosity dominated regime.

3.1.2 Large toughness asymptotic solution

As it has been done for the M vertex solution, I will report the K vertex scaling for the toughness-dominated regime. The system of equations can be written as

$$\Omega_{k0} = \left(\frac{3}{8\pi}\right)^{1/5} (1 - \rho^2)^{1/2}, \quad (3.8)$$

$$\Pi_{k0} = \frac{\pi}{8} \left(\frac{\pi}{12}\right)^{1/5} \simeq 0.3004, \quad (3.9)$$

$$\gamma_{k0} = \left(\frac{3}{\pi\sqrt{2}} \right)^{2/5} \simeq 0.8546. \quad (3.10)$$

The crack opening, Ω_{k0} , in the toughness-dominated regime as a function of the distance from the center of the fracture is shown in Figure 3.2. The dimensionless pressure, unlike the previous case, is constant with the increasing of the radial coordinate.

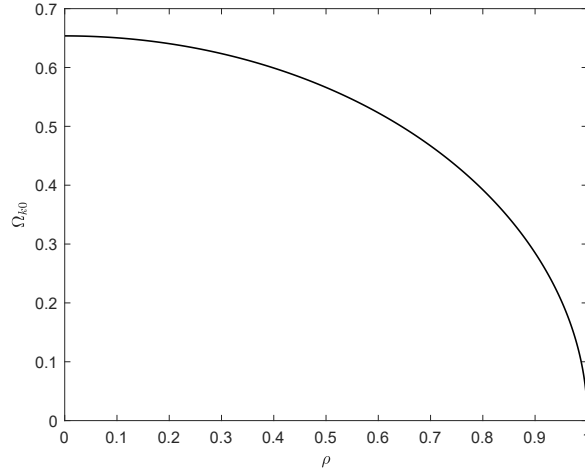


Figure 3.2: Crack opening in the toughness dominated regime.

3.1.3 Zero toughness–leak-off asymptotic solution

The \tilde{M} vertex solution describes the fracture propagating in a permeable medium with zero toughness, where the following expressions are valid

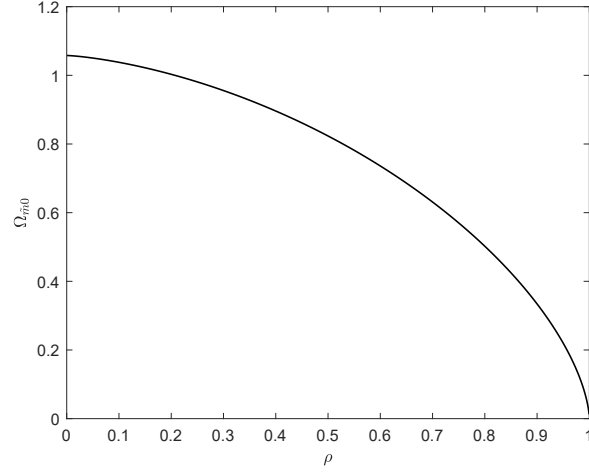
$$\gamma_{\tilde{m}0} = \frac{\sqrt{2}}{\pi}, \quad (3.11)$$

$$\begin{aligned} \Omega_{\tilde{m}0} = & \gamma_{\tilde{m}0} \left(D_1(1 - \rho^2)^{2/3} + D_2 \left(\sqrt{1 - \rho^2} - \rho \arccos \rho \right) \right) \\ & - \gamma_{\tilde{m}0} D_3 \left(\sqrt{1 - \rho^2} \int_0^1 {}_2F_1 \left(\frac{3}{8}, 1; \frac{3}{2}; (1 - \rho)^2 s^2 + \rho^2 \right) ds - 4\sqrt{1 - \rho^2} \right), \end{aligned} \quad (3.12)$$

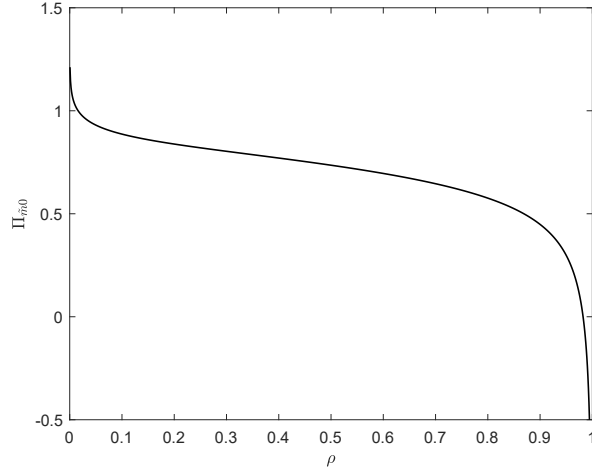
$$\Pi_{\tilde{m}0} = D_4 \left[4 - (1 - \rho^2)^{-3/8} \right] - D_5 [3(2\rho^2 - 1) - 1] + D_6 \left[\log \left(\frac{2}{\rho} \right) - 1 \right], \quad (3.13)$$

where $D_1 = 0.1146$, $D_2 = 0.3571$, $D_3 = 0.6611$, $D_4 = 0.2596$, $D_5 = 0.0169$, $D_6 = 0.1403$ and ${}_2F_1(\cdot)$ is the Gauss' hypergeometric function.

As it was done before, the trend of the crack opening and fluid pressure in the \tilde{M} -vertex solution over ρ are shown in Figure 3.3a and 3.3b.



(a)



(b)

Figure 3.3: Crack opening and net pressure in the viscosity–leak-off dominated regime.

The dimensionless pressure over the radial coordinate tends to infinite as ρ tends to zero; indeed it tends to minus infinite when ρ tends to one.

As observed in Paragraph 3.1.1, it is not possible to estimate the exact result of

the dimensionless pressure when $\rho = 0$ and $\rho = 1$.

3.1.4 Large toughness–leak-off asymptotic solution

The case of a radial hydraulic fracture propagating in a permeable medium characterized by large toughness describes the \tilde{K} -vertex solution, where the following expression are valid

$$\gamma_{\tilde{k}0} = \frac{\sqrt{2}}{\pi}, \quad (3.14)$$

$$\Pi_{\tilde{k}0} = \frac{\pi^{3/2}}{2^{15/4}}, \quad (3.15)$$

$$\Omega_{\tilde{k}0} = \frac{1}{2^{1/4}\pi^{1/2}}\sqrt{1-\rho^2}. \quad (3.16)$$

Figure 3.4 shows how the crack opening in the \tilde{K} -vertex solution evolves along the dimensionless radius ρ ; instead the dimensionless pressure is constant against ρ .

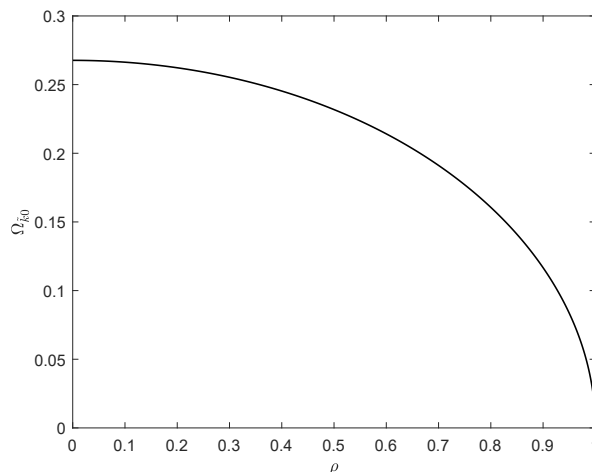


Figure 3.4: Crack opening in the toughness–leak-off dominated regime.

3.2 Time-based scaling

It is necessary to introduce the dimensionless times, which are summarized in Table 3.1, before describing the evolutions against the radial coordinate as time changes and as a function of the time itself.

All the evolution parameters, summarized in the Table 3.2, are useful to describe

Transition	Time scales	Dimensionless time τ
MK	$t_{mk} = \left(\frac{\mu'^5 E'^{13} Q_0^3}{K'^{18}} \right)^{1/2}$	$\tau_{mk} = t/t_{mk}$
$K\tilde{K}$	$t_{k\tilde{k}} = \left(\frac{K'^8 Q_0^2}{E'^8 C'^{10}} \right)^{1/3}$	$\tau_{k\tilde{k}} = t/t_{k\tilde{k}}$
$M\tilde{M}$	$t_{m\tilde{m}} = \left(\frac{\mu'^4 Q_0^6}{E'^4 C'^{18}} \right)^{1/7}$	$\tau_{m\tilde{m}} = t/t_{m\tilde{m}}$
$\tilde{M}\tilde{K}$	$t_{\tilde{m}\tilde{k}} = \frac{\mu'^4 E'^{12} C'^2 Q_0^2}{K'^{16}}$	$\tau_{\tilde{m}\tilde{k}} = t/t_{\tilde{m}\tilde{k}}$

Table 3.1: Dimensionless times equations.

each vertex solution; $\mathcal{K}_m, \mathcal{K}_{\tilde{m}}, \mathcal{M}_k, \mathcal{M}_{\tilde{k}}, \mathcal{S}_{\tilde{m}}, \mathcal{S}_{\tilde{k}}$ and $\mathcal{C}_m, \mathcal{C}_k$ have a meaning of a toughness, of a viscosity, of a storage or of a leak-off, respectively [11].

Scaling	ε	L	\mathcal{P}	
M	$\left(\frac{\mu'}{E't} \right)^{1/3}$	$\left(\frac{E'Q_0^3 t^4}{\mu'} \right)^{1/9}$	$\mathcal{K}_m = K' \left(\frac{t^2}{\mu'^5 Q_0^3 E'^{13}} \right)^{1/18}$	$\mathcal{C}_m = C' \left(\frac{E'^4 t^7}{\mu'^4 Q_0^3} \right)^{1/18}$
K	$\left(\frac{K'^6}{E'^6 Q_0 t} \right)^{1/5}$	$\left(\frac{E'Q_0 t}{K'} \right)^{2/5}$	$\mathcal{M}_k = \mu' \left(\frac{Q_0^3 E'^{13}}{K'^{18} t^2} \right)^{1/5}$	$\mathcal{C}_k = C' \left(\frac{E'^8 t^3}{K'^8 Q_0^3} \right)^{1/10}$
\tilde{M}	$\left(\frac{\mu'^4 C'^6}{E'^4 Q_0^2 t^3} \right)^{1/16}$	$\left(\frac{Q_0^2 t}{C'^2} \right)^{1/4}$	$\mathcal{K}_{\tilde{m}} = K' \left(\frac{t}{E'^{12} \mu'^4 C'^2 Q_0^2} \right)^{1/16}$	$\mathcal{S}_{\tilde{m}} = \left(\frac{\mu'^4 Q_0^6}{E'^4 C'^{18} t^7} \right)^{1/16}$
\tilde{K}	$\left(\frac{K'^8 C'^2}{E'^8 Q_0^2 t} \right)^{1/8}$	$\left(\frac{Q_0^2 t}{C'^2} \right)^{1/4}$	$\mathcal{M}_{\tilde{k}} = \mu' \left(\frac{E'^{12} C'^2 Q_0^2}{K'^{16} t} \right)^{1/4}$	$\mathcal{S}_{\tilde{k}} = \left(\frac{K'^8 Q_0^2}{E'^8 C'^{10} t^3} \right)^{1/8}$

Table 3.2: Evolution parameters equations

The relationship between scalings can be analyzed in Figure 3.5 with the rectangular parametric space $MK\tilde{K}\tilde{M}$; each vertex corresponds to a primary regime of the fracture propagation, that evolves with time t according to a power law [11]. A penny-shaped fracture starts its propagation from one of the four vertex solution and the trajectory that it will follow with the increasing of the time depends on the parameter ϕ that is defined as

$$\phi = \sqrt{\frac{t_{mk}}{t_{m\tilde{m}}}} = \frac{E'^{11/2} \mu'^{3/2} C'^2 Q_0^{1/2}}{K'^7} \quad (3.17)$$

The limit cases are

1. $\phi \ll 0$, formally $\phi = 0$;

2. $\phi \gg 0$, formally $\phi \rightarrow \infty$;

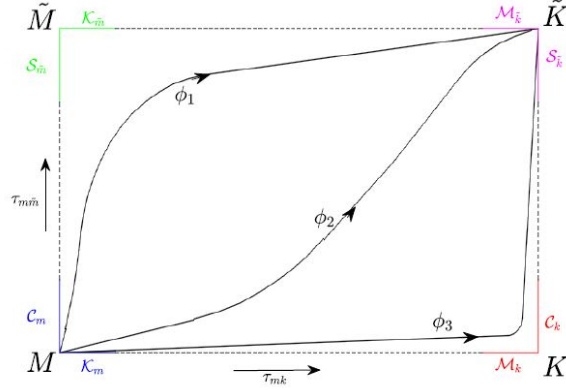


Figure 3.5: Rectangular phase diagram $MK\tilde{K}\tilde{M}$.

If the penny-shaped fracture starts its propagation from one of these two limit cases or close to them, then the crack propagation has always two possibilities of evolving; that depends either on the fluid (μ') or on the medium (K' , C'). If, e.g., the fracture falls in the case 1, the crack propagation can evolve along the storage-edge or along the toughness edge. Such possibility, will ultimately depend on both the C' value, if the medium is impermeable or not, and on the μ' value, if the fluid is inviscid or not [11].

Since the ϕ parameter is proportional to viscosity μ' and inversely proportional to toughness K' , it is easy to understand that as ϕ decreases, the trajectory follows the K -vertex and as ϕ increases, the trajectory follows the \tilde{M} -vertex.

3.2.1 Relationships between scalings

Each equation that describes the net pressure, the width of the fracture and the dimensionless radius (3.5)-(3.10) can be rewritten describing their evolution over the time (Table 3.3).

The evolution along the MK -edge of the crack radius γ (Figure 3.6a), the fracture opening Ω (Figure 3.6b) and the net pressure Π (Figure 3.6c) over the dimensionless time ($\tau = \tau_{mk}$) starts from the viscosity-storage dominated regime and reaches the storage-toughness dominated regime.

Considering the problem of fluid-driven radial fracture propagating in a permeable medium with zero toughness but with a relevant Carter's leak-off coefficient, the fracture will evolve along the $M\tilde{M}$ -edge.

In this case the relationships between the new scaling and the M and \tilde{M} scaling

	M	K
γ_{mk}	$\gamma_{m0}\tau^{4/9}$	$\gamma_{k0}\tau^{2/5}$
Π_{mk}	$\Pi_{m0}(\rho)\tau^{1/3}$	$\Pi_{k0}\tau^{-1/5}$
Ω_{mk}	$\Omega_{m0}(\rho)\tau^{1/9}$	$\Omega_{k0}\tau^{1/5}$

Table 3.3: Π_{mk} , Ω_{mk} and γ_{mk} depending on τ along MK -edge

are summarized in Table 3.4.

	M	\tilde{M}
$\gamma_{m\tilde{m}}$	$\gamma_{m0}\tau^{4/9}$	$\gamma_{\tilde{m}0}\tau^{1/4}$
$\Pi_{m\tilde{m}}$	$\Pi_{m0}(\rho)\tau^{1/3}$	$\Pi_{\tilde{m}0}\tau^{-3/16}$
$\Omega_{m\tilde{m}}$	$\Omega_{m0}(\rho)\tau^{1/9}$	$\Omega_{\tilde{m}0}(\rho)\tau^{1/16}$

Table 3.4: $\Pi_{m\tilde{m}}$, $\Omega_{m\tilde{m}}$ and $\gamma_{m\tilde{m}}$ depending on τ along $M\tilde{M}$ -edge

As done for MK -edge, the evolution of the fracture parameters at the injection point over the dimensionless time $\tau_{m\tilde{m}}$ is showed in Figure 3.7.

As expected, fracture radius, wellbore opening and fluid pressure evolve from the M - to the \tilde{M} -vertex solution with the increasing of the time.

3.3 Conclusions

Regarding the MK -edge solution, the problem considered regards a penny-shaped hydraulic fracture propagating in an impermeable medium: Carter’s leak-off is null or in any case negligible. Since $C' \approx 0$, it is easy to deduce from Table 3.2 that the fracture propagation can evolve proportionally to a power of time itself: $\tau^{1/9}$ and $\tau^{-2/5}$.

As Madyarova demonstrates [11], in the limiting case of null Carter’s leak off, the evolution of the fracture from M to K vertex solution is completely controlled by the tip asymptote.

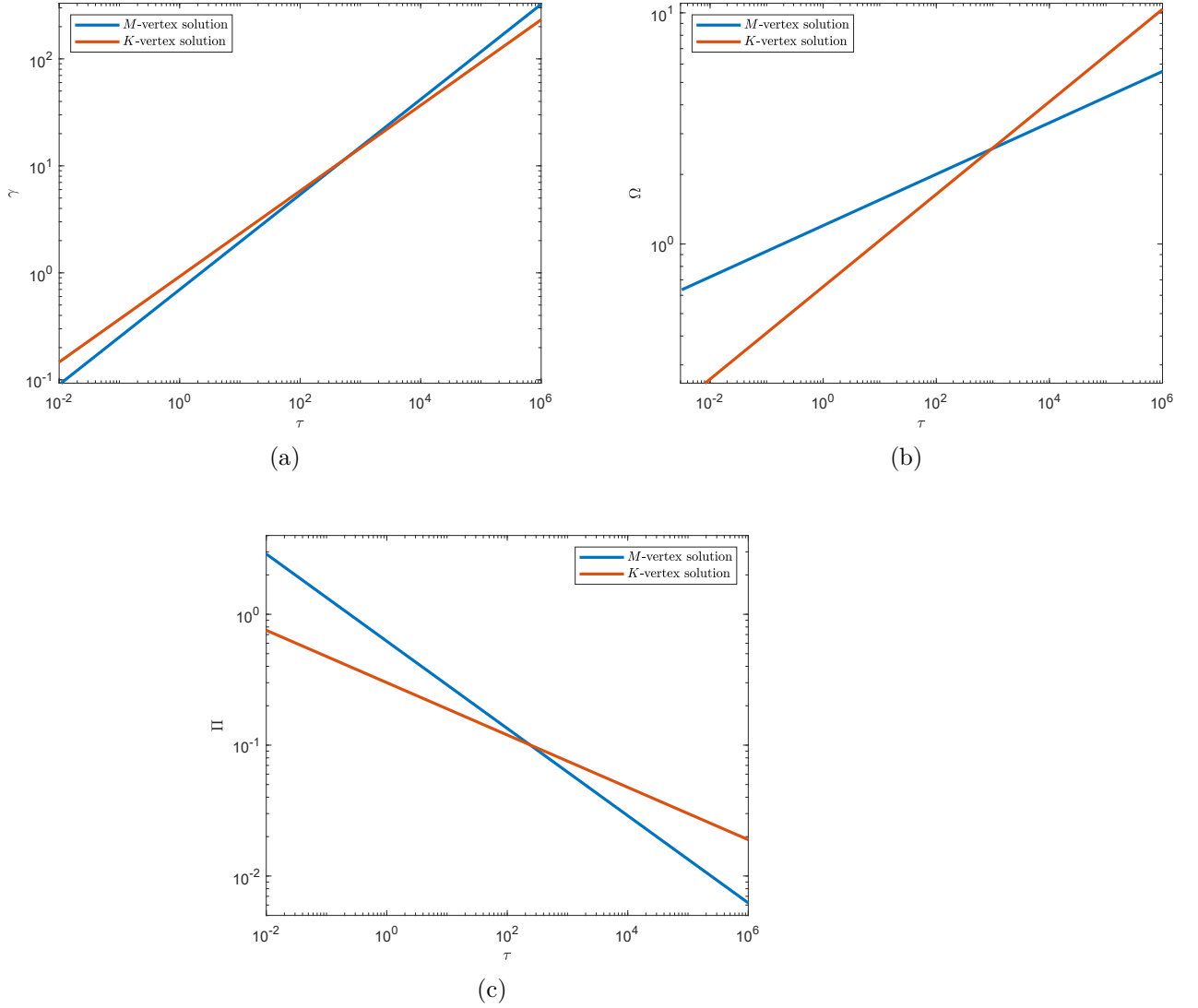


Figure 3.6: Crack opening, net pressure and fracture radius over the dimensionless time. Π is calculated in $\rho = 0.5$ and Ω is calculated at the first node.

Figure 3.6 illustrates that the solutions for γ , Ω and Π start from the viscosity-storage dominated regime and reaches the storage-toughness dominated regime, as it is expected, passing through a mixed-regime, where the solution depends on both the viscosity and the toughness.

Considering the case of a radial fracture propagating in a permeable medium characterized by negligible toughness but not negligible leak-off, the fracture propagates

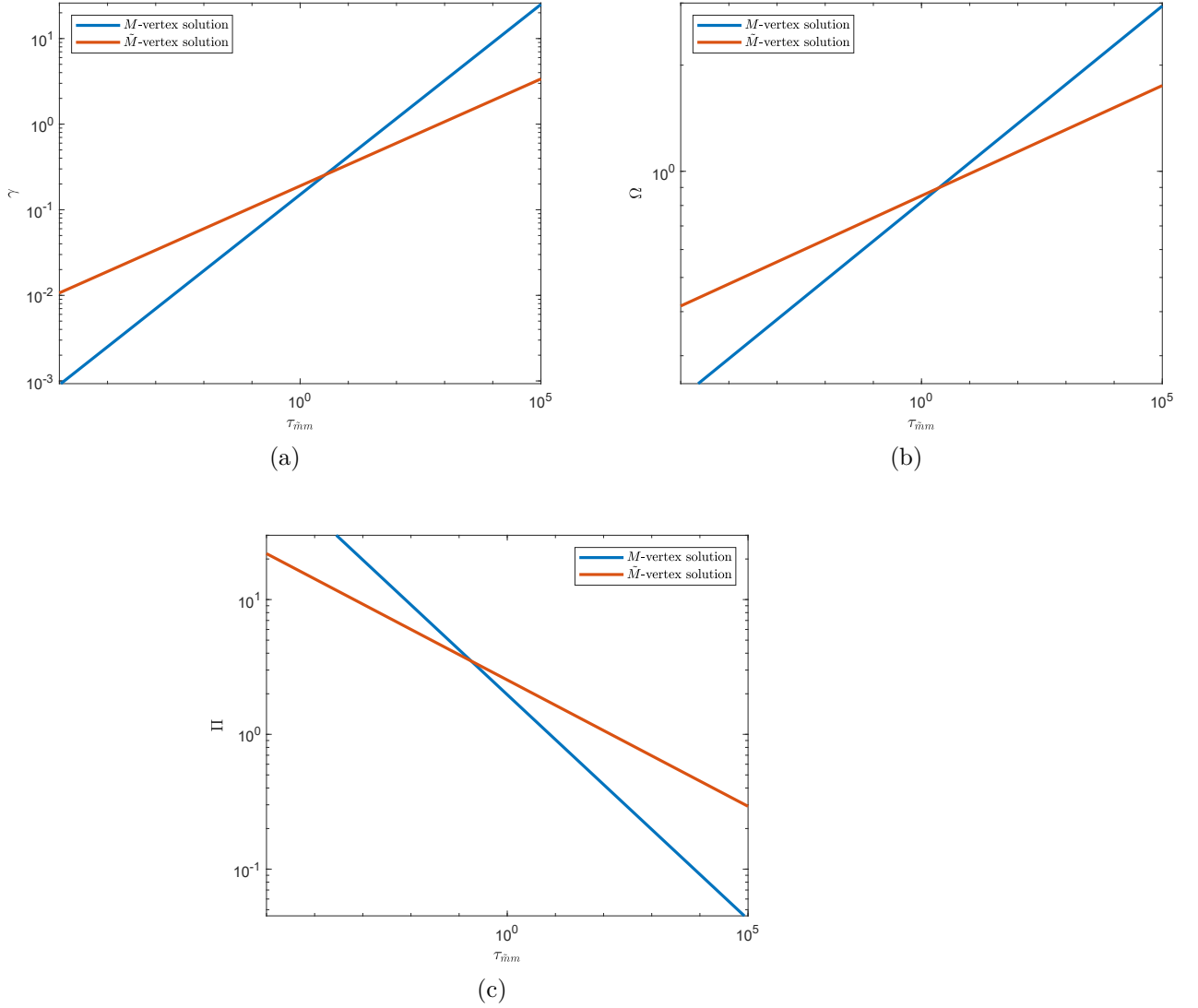


Figure 3.7: Crack opening, net pressure and fracture radius over the dimensionless time. Π is calculated in $\rho = 0.5$ and Ω is calculated at the first node.

along the $M\tilde{M}$ -edge. In this case the evolution of the parameter over the time follows $\tau^{7/18}$ and $\tau^{-7/16}$.

As it is shown in Figures 3.7, the radius, the width and the pressure at the node near the inlet pass from the M -vertex solution to the \tilde{M} -vertex solution with the increasing of the dimensionless time (Figure 3.5).

Vertex solutions are useful to estimate the structure of the fracture at one instant of time in terms of fracture radius and wellbore width, as shown in Figure 3.8; the

height (H) is chosen equal to the 20% of the fracture radius.

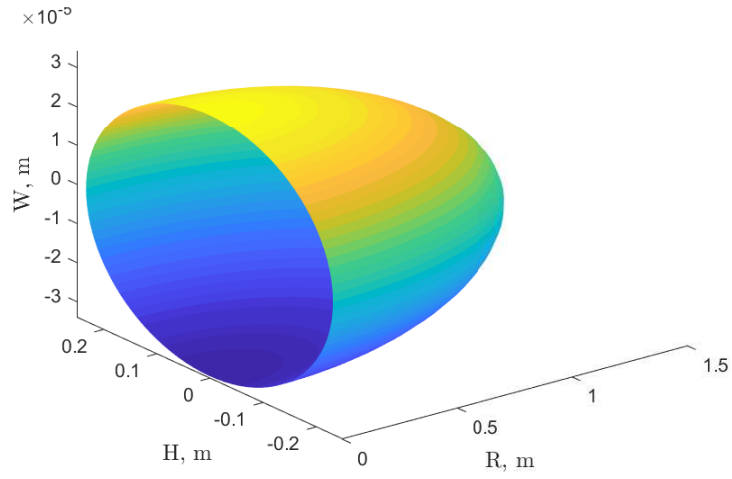


Figure 3.8: Design fracture after 1 second.

Figure 3.5 is helpful to know a priori what is the evolution of the system's variables with the increasing of time, based on the knowledge of all of the parameters that describe the system.

Chapter 4

Approximate solution for a penny shaped hydro-fracture

The solution reported in this chapter follows the previous work of Dontsov [5], where the author defines the approximation for the fracture width as

$$w(r, t) = \left(\frac{R+r}{2R} \right)^\lambda w_a(R-r), \quad (4.1)$$

where w_a is the tip asymptotic solution, that depends either on material parameters and on the distance from a point inside the fracture to the tip ($s = R - r$) as well, and λ is a parameter that will be defined in Paragraph 4.2.

The tip region is defined as $(R - r)/R \ll 1$ and here, as it is shown in [14], the governing equations are identical to the equations for the problem of a semi-infinite fluid driven fracture which is propagating at a constant velocity in zero-lag conditions. Indeed close to the tip of a shaped fracture with a smooth front, the governing equations reduce to those for a semi-infinite hydraulic fracture propagating at a constant velocity.

Since $w_a(s)$ is proportional to $\alpha^{\bar{\delta}}$, where $\bar{\delta}$ is a slowly varying function, and using the ρ term introduced in Chapter 2.2, Equation 4.1 can be reduced to

$$w(r, t) = \left(\frac{1+\rho}{2} \right)^\lambda (1-\rho)^{\bar{\delta}} w_a. \quad (4.2)$$

It is assumed that $R(t)$ is proportional to t^α , where *alpha* is a slowly varying function and it can assume the value of 1/4, 2/5 or 4/9, as shown in Table 3.2 depending on which vertex-solution is considered. Considering the global fluid balance (Equation 2.5) and equation 4.2 leads to

$$w_a(R)2^{1+\bar{\delta}} \left[B_0 \left(\frac{1}{2}; \lambda + 2, \bar{\delta} + 1 \right) - B_0 \left(\frac{1}{2}; \lambda + 1, \bar{\delta} + 2 \right) \right] + 2C't^{1/2}\alpha B \left(2\alpha, \frac{3}{2} \right) = \frac{Q_0 t}{2\pi R^2}, \quad (4.3)$$

where the beta function follows

$$B_0(x; a, b) = \int_x^1 t^{a-1}(1-t)^{b-1} dt = B(a, b) - B(x; a, b), \quad (4.4)$$

and $B(x; a, b)$ is the incomplete beta function.

Regarding the fluid pressure, replacing the Equation 4.1 in 2.2, it can be written as

$$p = \frac{E'w_a}{R} \mathcal{F}(\lambda, \bar{\delta}, \rho), \quad \mathcal{F}(\lambda, \bar{\delta}, \rho) = \frac{1}{2^{1+\lambda}\pi} \int_0^1 \frac{\partial M(\rho, s)}{\partial s} (1+s)^\lambda (1-s)^{\bar{\delta}} ds, \quad (4.5)$$

where the kernel $M(\rho, s)$ is defined in Equation 2.3 and the function $\mathcal{F}(\lambda, \bar{\delta}, \rho)$ can be evaluated numerically.

It is important to introduce the efficiency defined as the ratio between the volume of the fluid that remains within the fracture and the total volume of the injected fluid [5] and it can be calculated as

$$\eta(t) = \frac{2^{2+\bar{\delta}}\pi R^2 w_a(R)}{Q_0 t} \left[B_0\left(\frac{1}{2}; \lambda + 2, \bar{\delta} + 1\right) - [B_0\left(\frac{1}{2}; \lambda + 1, \bar{\delta} + 2\right)] \right]. \quad (4.6)$$

It depends on the fracture radius, the opening at the tip, the flow rate and on the terms λ and $\hat{\delta}$ that are in the B function as well.

4.1 Solution in scaled variables

As shown in [6] and [7], the fracture width, the fluid pressure and the efficiency can be expressed using the following scaled terms

$$\hat{s} = \frac{\mu' \alpha R^3}{t E' w_a^3} = g_\delta(\hat{K}, \hat{C}), \quad \hat{K} = \frac{K' R^{1/2}}{E' w_a}, \quad \hat{C} = \frac{2C' t^{1/2}}{\alpha^{1/2} w_a}, \quad (4.7)$$

that, associated with

$$t^* = \frac{K'^{12} E'^{-10}}{\mu'^2 (2C')^6}, \quad R^* = \frac{K'^{10} E'^{-8}}{\mu'^2 (2C')^4}, \quad w_a^* = \frac{K'^6 E'^{-5}}{\mu' (2C')^2}, \quad Q_0^* = \frac{2\pi K'^{14} E'^{-11}}{\mu'^3 (2C')^4}, \quad p^* = \frac{\mu' (2C')^2}{K'^4 E'^{-4}}, \quad (4.8)$$

can be used to convert the solution to the unscaled form:

$$\hat{t} = \frac{t}{t^*}, \quad \hat{R} = \frac{R}{R^*}, \quad \hat{w}_a = \frac{w_a}{w_a^*}, \quad \hat{Q}_0 = \frac{Q_0}{Q_0^*}, \quad \hat{p} = \frac{p}{p^*}, \quad (4.9)$$

where

$$\hat{w}_a = \frac{\hat{C}^2 \hat{s}}{2^2 \phi^{1/2}}, \quad \phi' = \frac{\mu'^3 E'^{13} C'^4 Q_0}{K'^{14}}, \quad (4.10)$$

$$\hat{p}(\rho, \hat{t}) = \frac{\hat{w}_a(\hat{t})}{\hat{R}(\hat{t})} \mathcal{F}(\lambda, \bar{\delta}, \rho), \quad (4.11)$$

$$\hat{w} = \left(\frac{1 + \rho}{2} \right)^\lambda (1 - \rho)^{\bar{\delta}} \hat{w}_a(\hat{t}), \quad (4.12)$$

and, comparing the relation that defines ϕ' (Equation 4.10) with Equation 3.17, it is easy to deduce that $\phi' = \phi^2$.

As regard the efficiency, it can be rewritten using the scaled form as follow

$$\eta(\hat{t}) = 1 - \frac{\hat{C} \alpha^{3/2} B \left(2\alpha, \frac{3}{2} \right)}{\mathcal{B}(\hat{K}, \hat{C}, \alpha)}, \quad (4.13)$$

where

$$\mathcal{B}(\hat{K}, \hat{C}, \alpha) = \frac{\alpha \hat{Q}_0 \hat{K}^{14}}{\hat{C}^4 \hat{\mathfrak{S}}^3}. \quad (4.14)$$

The radius of the fracture is defined as

$$R = \gamma L, \quad (4.15)$$

where

$$\gamma = \frac{\hat{R}}{2^4 \phi'}, \quad L = \left(\frac{Q_0^3 E' t_{mk}^4}{\mu'} \right)^{1/9}. \quad (4.16)$$

4.2 Numerical algorithm

Using the Equations 4.7, 4.8 and 4.14 that define \hat{s} , \hat{t} and B respectively, it is possible to obtain the system of equations

$$\begin{cases} \alpha^{1/2} \hat{C}^3 g_\delta(\hat{K}, \hat{C}) - \hat{t}^{1/2} \hat{K}^6 = 0 \\ \hat{t}^{3/2} \hat{K}^4 \mathcal{B}(\hat{K}, \hat{C}, \alpha) - \alpha^{5/2} \hat{Q}_0 \hat{C}^5 = 0. \end{cases} \quad (4.17)$$

The system is solved using Newton–Raphson method and the initial value of α is equal to 4/9, than the correct value is found iteratively using

$$\alpha = \frac{\partial \log(\hat{R})}{\partial \log(\hat{t})}. \quad (4.18)$$

Since \hat{K} , \hat{C} and α are not unknowns anymore, it is possible to find λ using the following interpolation procedure:

$$\lambda(\hat{K}, \hat{C}, \alpha) = \lambda_m (1 - \hat{K}^4) \eta_0 + \lambda_{\bar{m}} (1 - \hat{K}^4) (1 - \eta_0) + \lambda_{\bar{k}} \hat{K}^4 (1 - \eta_0), \quad (4.19)$$

where η_0 is the approximation for the efficiency (Equation 4.6) for which $\lambda = 0.5$, and, using a comparison between the approximate solution and the vertex solution, Dontsov [5] defines $\lambda_m = 0.487$, $\lambda_k = \lambda_{\bar{k}} = 0.55$ and $\lambda_{\bar{m}} = 0.397$.

Interpolating as in Equation 4.19 guarantees the correct value of λ in the four vertices and a good approximation elsewhere; this will be verified in Paragraph 4.3.

4.3 Time-based scaling

Using the dimensionless time (Table 3.1) and the leak-off parameter, defined in the equations below, the map in Figure 4.1 is constructed to determine the regime of propagation or the possible time evolution paths; it indicates the areas of applicability of the limiting solutions. The boundaries of each transition have been

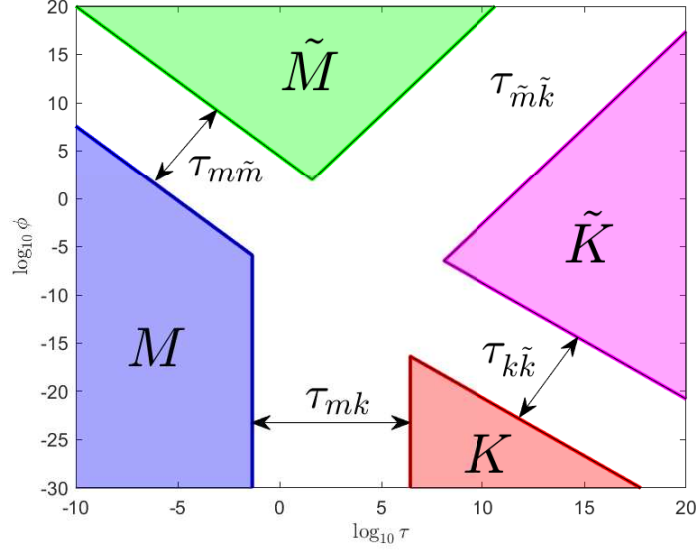


Figure 4.1: Variation of the approximate solution versus dimensionless time and the leak-off parameter.

calculated numerically and summarized in the Table 4.1.

Edge	τ at the beginning of the transition	τ at the end of the transition
$M - K$	$\tau_{mk} \simeq 4.54 \cdot 10^{-2}$	$\tau_{mk} \simeq 2.59 \cdot 10^6$
$M - \tilde{M}$	$\tau_{m\tilde{m}} \simeq 7.41 \cdot 10^{-6}$	$\tau_{m\tilde{m}} \simeq 7.20 \cdot 10^2$
$K - \tilde{K}$	$\tau_{k\tilde{k}} \simeq 5.96 \cdot 10^{-8}$	$\tau_{k\tilde{k}} \simeq 4.81 \cdot 10^2$
$\tilde{M} - \tilde{K}$	$\tau_{\tilde{m}\tilde{k}} \simeq 4.18$	$\tau_{\tilde{m}\tilde{k}} \simeq 2.01$

Table 4.1: Value of the dimensionless time along each edge.

It is possible to check the accuracy of the approximate solutions comparing it with

the vertex solution analyzed above.

As it is shown in Figure 4.2, analyzing the dimensionless fracture radius, wellbore width and fluid pressure, the approximate solution evolves from the M - to the K -vertex solution, because the leak-off parameter is constant and it is negligible.

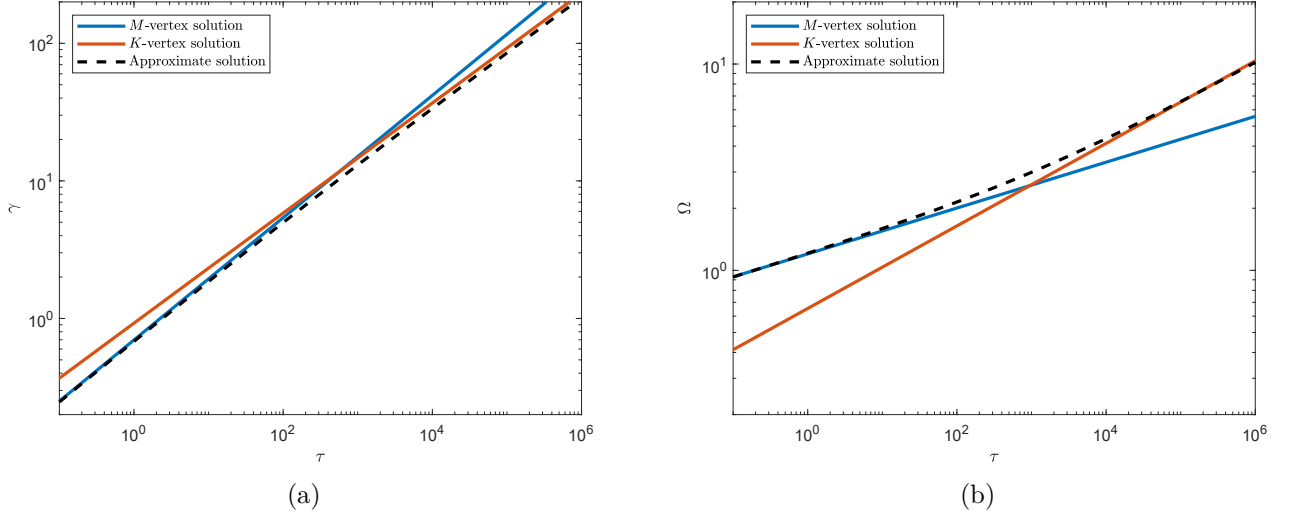


Figure 4.2: Comparing approximate solution with M - and K -vertex solution of the crack opening, net pressure and fracture radius over the dimensionless time. Π is calculated in $\rho = 0.5$ and Ω is calculated at the first node.

In the same way, using a constant leak-off parameter not negligible anymore, Figure 4.3 compares the approximate and the numerical solution calculated along the $M\tilde{M}$ edge.

The Figure 4.4 shows the error between the vertex solutions and the analytical ones along both in MK edge and the $M\tilde{M}$ edge, that is calculated as

$$Error = \sqrt{\left| \left[\frac{X_{appr} - X_{num}}{X_{appr}} \right]^2 \right|}, \quad (4.20)$$

where X is either the fracture radius, the wellbore width or the pressure and subscripts “Appr” and “Num” indicate the approximation and numerical solution, respectively. The maximum value of the error is reached from the dimensionless pressure along the $M\tilde{M}$ edge and it is equal to 0.3632; the pressure is less accurate because the elasticity integral, used to calculate it, is very sensitive to the fracture width profile. However, this is the proof that the interpolation procedure for λ is sufficiently accurate [5].

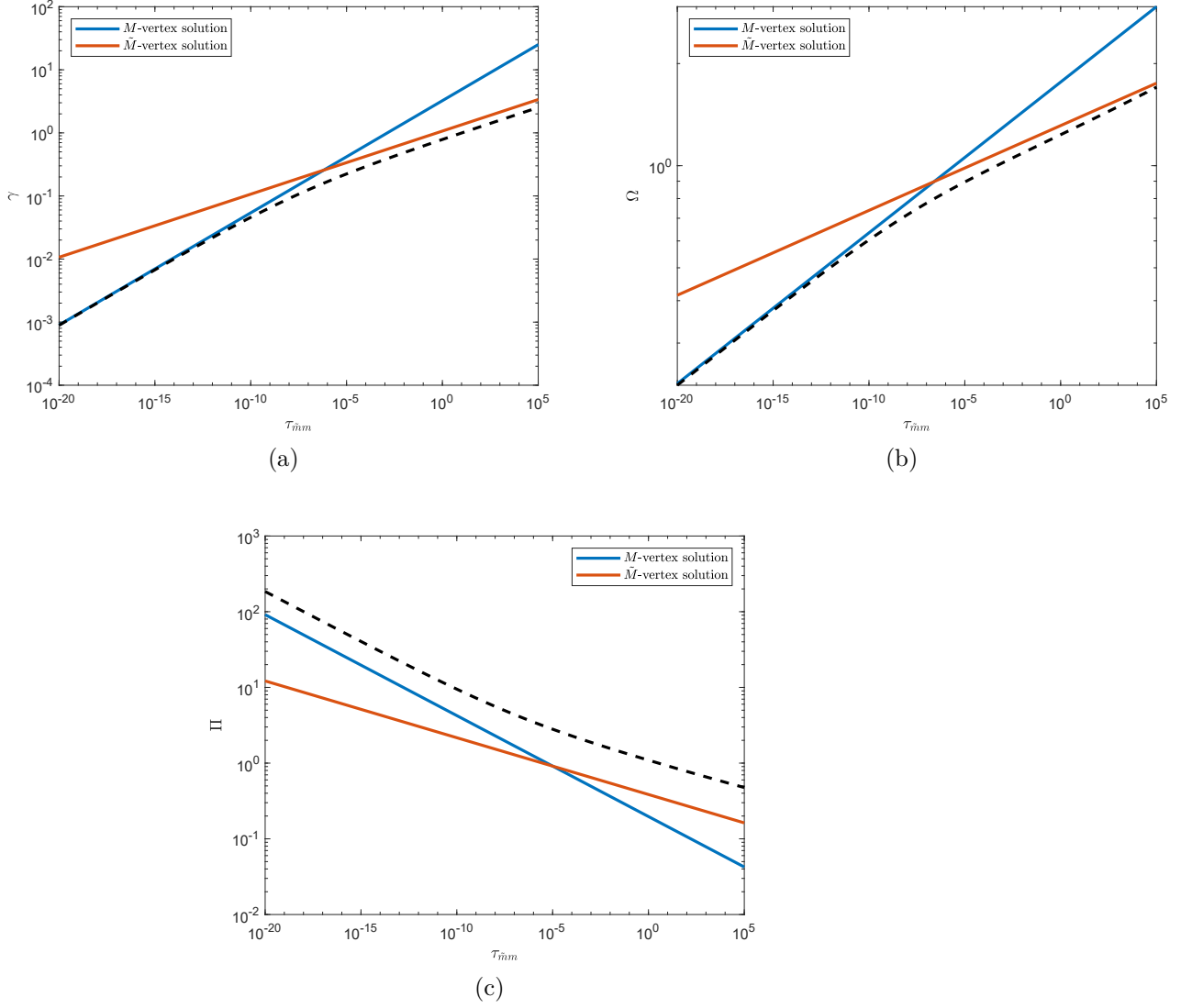


Figure 4.3: Comparing approximate solution with M - and \tilde{M} -vertex solution of the crack opening, net pressure and fracture radius over the dimensionless time. Π is calculated in $\rho = 0.5$ and Ω is calculated at the first node.

4.3.1 Comparison with numerical solution

It is possible to verify that the approximate solution studied by Dontsov evolves along ρ from one vertex solution to another with increasing dimensionless time, keeping the leak-off parameter constant.

In Figures 4.5a and 4.5b, all the system's parameters have been chosen in order to obtain $\phi' = 10^{-20}$; this guarantees, as shown in Figure 4.5c, that the approximate

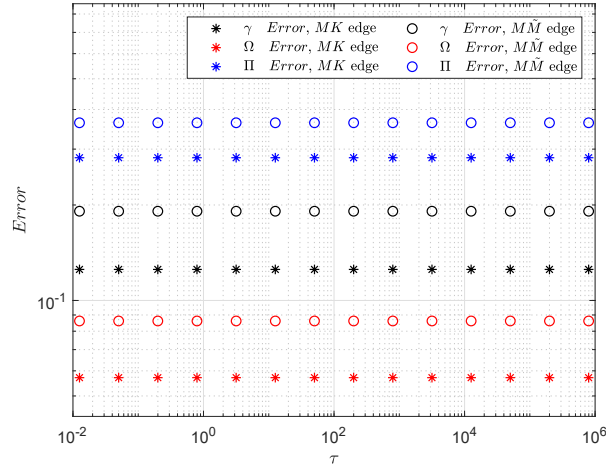


Figure 4.4: Interpolation of the error's results in logarithmic scale between numerical and approximate solution.

solution evolves from the M - to the K -vertex solution when the dimensionless time goes from 10^2 to 10^7 .

Figures 4.6a and 4.6b show the transition from the M - to the \tilde{M} - vertex solution, considering $\phi' = 10^4$ and the dimensionless time between 10^{-5} and 10^3 . These graphics allow to verify the approximate solution and its evolution from the zero toughness to the zero toughness–leak-off asymptotic solution.

Figure 4.5c and 4.6c are included to show what is the path that the approximate solution should follow in a given time frame.

It is now possible to study the evolution of the efficiency η for both the MK transition and $M\tilde{M}$ transition. In Figures 4.7a it is possible to notice, referring to the data used in Figure 5.4, that the efficiency does not decrease a lot: it starts from the M vertex with an efficiency ideally equal to 1 and it reaches the value of 99% when it arrives to the K vertex solution.

Concerning Figure 4.7b, the difference with the efficiency in the MK transition, is the evident reduction in the $M\tilde{M}$; indeed at the end of the viscosity regime the efficiency is 98% and, going towards the viscosity regime, its value reaches 2%.

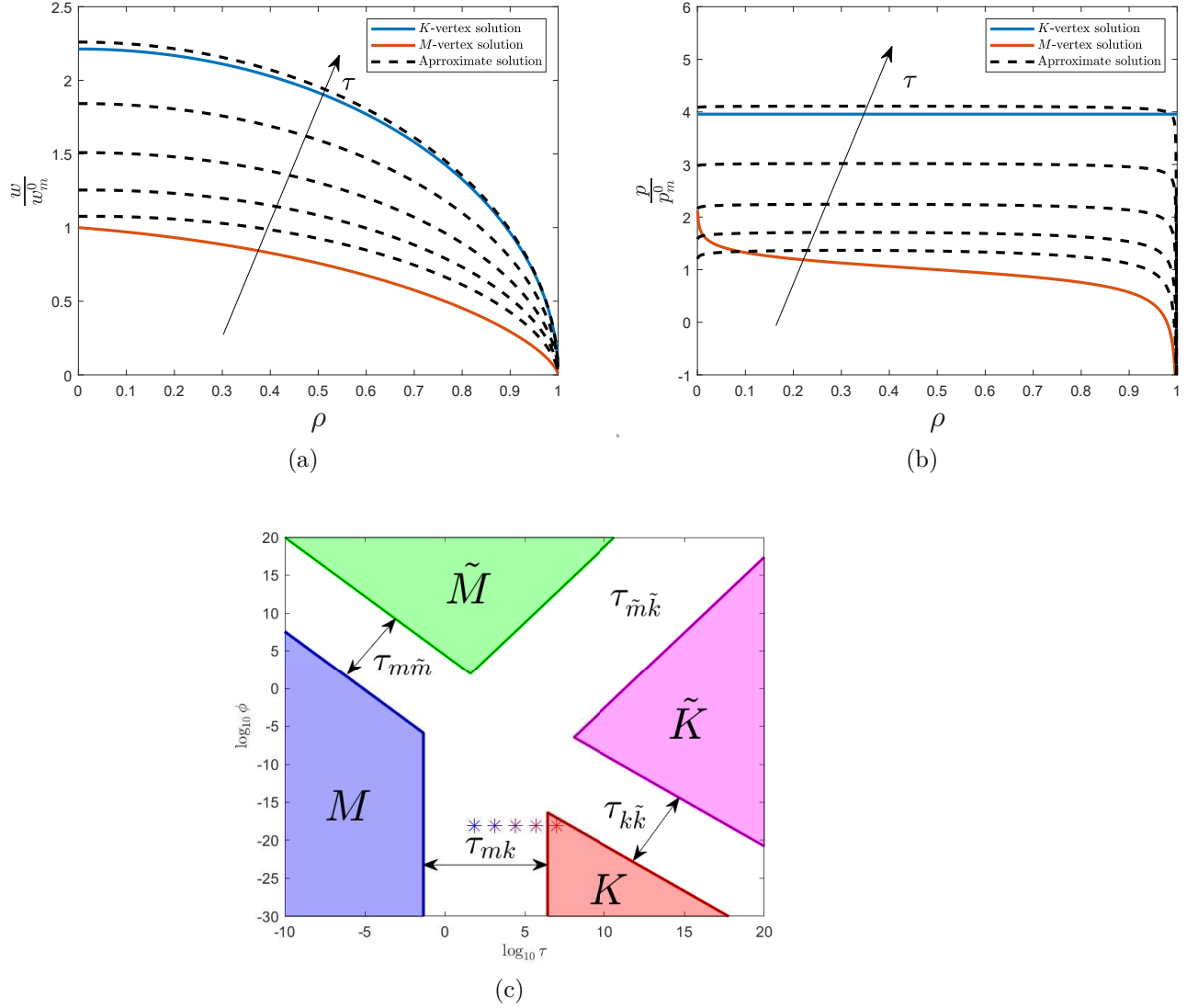


Figure 4.5: Comparing approximate solutions in different instant times, with vertex solutions of the crack opening over the dimensionless radius. Width and pressure are normalized by the M -vertex solution calculated in $\rho = 0$ and $\rho = 0.5$, respectively.

4.4 Conclusions

The M and K -vertex asymptotes were included to demonstrate that the numerical solution starts from the viscosity-storage dominated regime and reaches the storage-toughness dominated regime with the increasing of the time, as it is expected and the approximate solution can follow for both Ω and Π the time increasing.

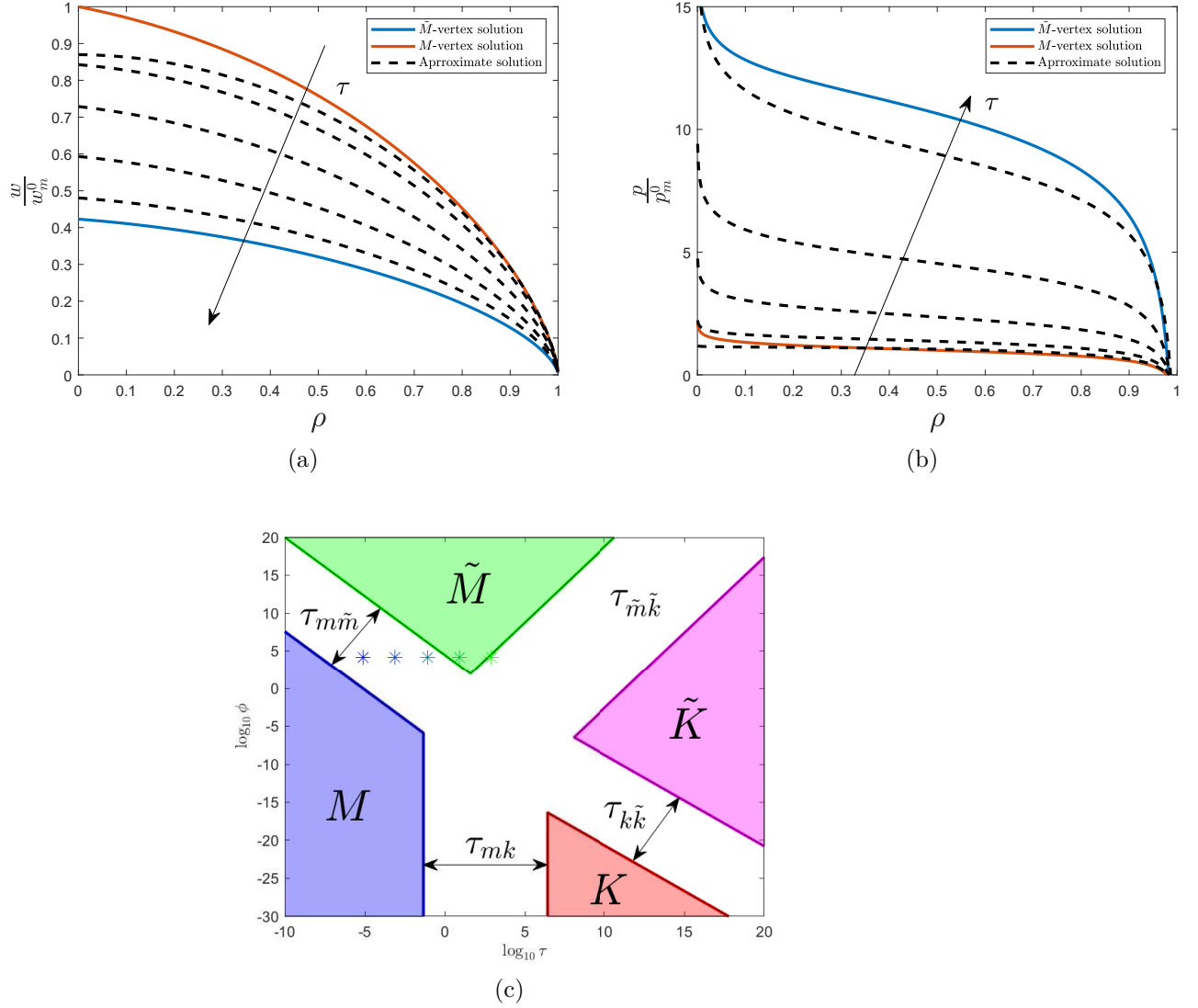


Figure 4.6: Comparing approximate solutions in different instant times, with vertex solutions of the crack opening over the dimensionless radius. Width and pressure are normalized by the M -vertex solution calculated in $\rho = 0$ and $\rho = 0.5$, respectively.

The M and \tilde{M} -vertex solutions have been plotted to show that the numerical solution evolves from the viscosity-storage dominated regime to the viscosity-leak-off dominated regime and the approximate solution evolves following the way highlighted in Figure 4.6c, as expected. It is possible to notice that all the transitions from one asymptote to another are very smooth.

Fracture width variations are accurate, indeed the logarithmic error (Figure 4.4) is

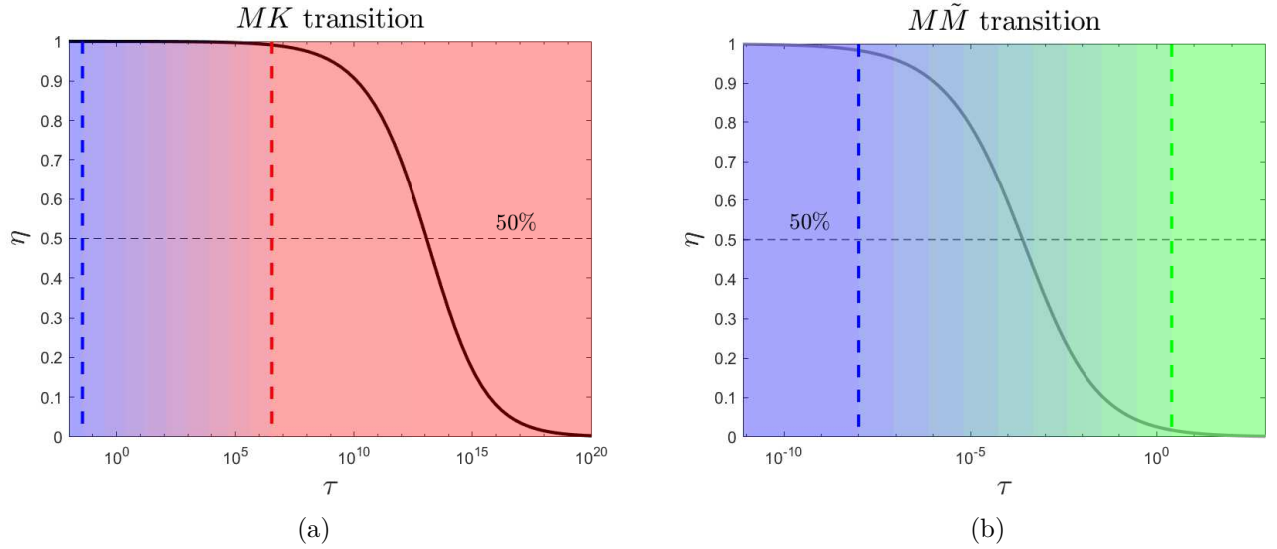


Figure 4.7: Efficiency over the dimensionless time in MK and in MM edge.

the lower, whereas the fluid pressure estimations are farther away from the vertex solutions the closer they are to the tip; Dontsov suggest that it should not be used to evaluate pressure for $\rho \geq 0.8$.

Certainly the approximate solution, together with the map in Figure 4.1, can be used to estimate the fracture radius and for a rapid fracture design calculation; instead imposing the height of the fracture equal to 0.2 times the fracture radius, in Figure 4.8 it is possible to notice the difference between the numerical and the approximate solution in the structure of the fracture after 1 second.

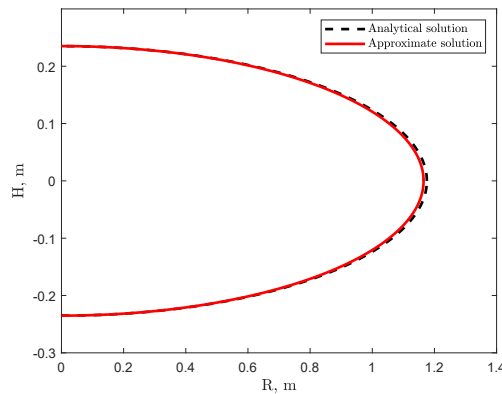


Figure 4.8: Fracture design comparing numerical and approximate solution after $t = 1s$.

The map in Figure 4.1 allows to know which vertex solution best describes fracture design and fluid pressure at any time.

Chapter 5

Application to geothermal case study

The Acozulco geothermal zone is located in a volcanic complex in the trans-mexican volcanic belt, Mexico. Two exploring wellbores were drilled in the '80s: *EAC1* and *EAC2*, shown in Figure 5.1, after [13]. This site is characterized as a possible site for a Hot Dry Rock (HDR) project because of the high temperature originating from the heat source related to a volcano-tectonic processes and because of the low permeability of the host rocks.

The Dontsov's analytical solution of hydro-fracture has been applied on these case studies, calculating the radius of the fracture in each depth and the corresponding energy and efficiency to estimate which is the optimal depth for hydraulic fracturing.

5.1 Numerical model

The idealized stratigraphy is built after the work of Pulido et al. [15] and Calcagno et al. [2].

We have considered stimulation scenarios for the two existing wellbores, *EAC1* and *EAC2* and exclusively between 1 and 3 km depth. The model parameters were obtained experimentally from tests performed at outcrop of the Skarns and Marbles from Acozulco (B. Lpillier and J. Kummerow, personal communication). Values are indicated in Tables 5.1 and 5.2 and in Figure 5.2.

The wellhead temperature is 50°C and the geothermal gradient is 0.13° C/m and 0.11° C/m for, respectively, *EAC1* and *EAC2* (Figure 5.3). The hydrostatic pressure is computed taking into account density variation of water with temperature and pressure. The properties of water such as density, specific heat, viscosity are

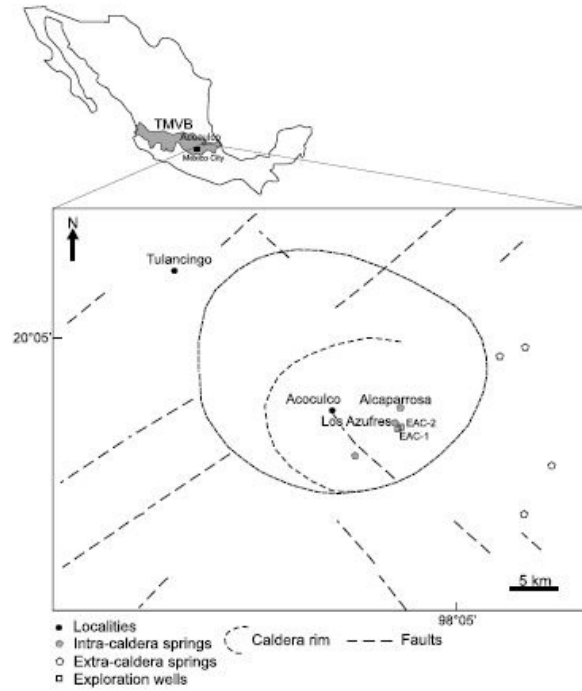


Figure 5.1: Location of the Acoculco geothermal zone [13].

Lithology	Depth,	Permeability,	Young's modulus,	Poisson's ratio	Porosity	
	m	$1/m^2$	Pa			
Volcanites	0	–790	$1 \cdot 10^{-17}$	$4 \cdot 10^{10}$	0.2	0.02
Skarn	–790	–1200	$2.2 \cdot 10^{-16}$	$5.76 \cdot 10^{10}$	0.1	0.05
Marble	–1200	–1300	$1.21 \cdot 10^{-18}$	$5.2 \cdot 10^{10}$	0.3	0.025
Skarn	–1300	–1650	$2.25 \cdot 10^{-16}$	$5.76 \cdot 10^{10}$	0.1	0.05
Granite	–1650	–3000	$1 \cdot 10^{-19}$	$7 \cdot 10^{10}$	0.25	0.02

Table 5.1: EAC1 model parameters.

computed with the external library **freesteam** (<http://freesteam.sourceforge.net/>), which is based on the IAPWS-97 standard for the thermodynamic properties of water and steam.

Lithology	Depth,	Permeability,	Young's modulus,	Poisson's ratio	Porosity	
	m	$1/m^2$	Pa			
Volcanites	0	–450	$1 \cdot 10^{-17}$	$4 \cdot 10^{10}$	0.2	0.02
Skarn	–450	–1750	$2.25 \cdot 10^{-16}$	$5.76 \cdot 10^{10}$	0.1	0.05
Granite	–1750	–3000	$1 \cdot 10^{-19}$	$7 \cdot 10^{10}$	0.25	0.02

Table 5.2: EAC2 model parameters.

Figures ?? and ?? show the cross-section used for modelling the two wellbores with the respective materials for each depth.

Concerning the Carter's leak-off coefficient, it has been calculated as [9] (Appendix A)

$$C_L = \Delta p \sqrt{\frac{k\varphi c_t}{\mu\pi}}, \quad (5.1)$$

where k is the permeability, φ the porosity and c_t is the total compressibility that has been approximate as

$$c_t \simeq c_1, \quad (5.2)$$

where c_1 is the isothermal fluid compressibility; Δp is the pressure drop calculated as the difference between p_c and p_0 that are defined as

$$\begin{cases} p(0, t) = p_c, & t > 0 \\ p(\infty, 0) = p_0, & x \geq 0. \end{cases} \quad (5.3)$$

Indeed, considering an infinite homogeneous and isotropic porous medium, it is located at the positive part of x axis, instead the interface between the medium and the fracture is located at $x = 0$. p_c on the interface keeps constant since time $t = 0$ and p_0 is the fluid pressure within the medium everywhere.

The pressure depends on the leak-off coefficient and the Carter's leak-off coefficient depends on the pressure itself; for this reason it was necessary to iterate with the Newton–Raphson method using a Carter's leak off coefficient equal to $1 \cdot 10^{-6} m/s^{1/2}$ as initial value and it was necessary to set $1 \cdot 10^7$ Pa as maximum value of Δp ; the obtained results are shown in Figure 5.5.

In order to take into account the thermal effects of temperature on the fracturing behaviour of rocks, this study includes a temperature-dependent law of toughness.

The model is empirical and it is based on fracture mechanics experiments on granite and gabbro available in the literature [12]. We have compiled the values of fracture toughness with temperature $K_I(T)$, and normalized it to the value of toughness at ambient temperature

$$\hat{K}_I(T) = \frac{K_I(T)}{K_I(T = 20^\circ C)} \quad (5.4)$$

Interpolating the experimental data, we found the best empirical relation that approximates the evolution of fracture toughness with temperature is given by

$$\hat{K}_I(T) = \frac{a_1 + a_2 T}{1 + a_3 T + a_4 T^2} \quad (5.5)$$

with coefficients $a_1 = 9.50 \times 10^{-1}$, $a_2 = 1.86 \times 10^{-3}$, $a_3 = -9.20 \times 10^{-4}$ and $a_4 = 1.57 \times 10^{-5}$ calibrated based on the experiments on gabbro and granite [12]. Figure 5.6 shows how the \hat{K} term evolves with increasing temperature, comparing experimental and interpolated results.

5.2 Results

5.2.1 Fracture radius

Following the Equation 4.15, it is possible to calculate the fracture radius in each depth, considering a flow rate equal to $0.08m^3/s$ at time $t = 7200s$. Figure 5.7 shows the results regarding both wells EAC1 and EAC2.

It is evident how the Carter's leak-off influences the fracture radius trend: the two quantities are inversely proportional. This behaviour is confirmed by the leak-off definition: loss of fracturing fluid into the permeable rock.

5.2.2 Efficiency

Knowing the fracture radius and the Equation 4.13, it is possible to calculate the efficiency of the system in one specific instant time and it is shown in Figure 5.8. Therefore, the efficiency's results obtained for each well show the inverse proportionality between the energy and the Carter's leak-off; this is exactly what was expected from the Equation 4.13, precisely because the efficiency and the square of the fracture radius turned out to be directly proportional.

5.3 Influence of the rock and fluid’s parameters on the radius

It is possible to study how the rock and fluid’s parameters influence the fracture radius and system’s efficiency.

5.3.1 Flow rate

In general, the lower the injection rate, the longer time it takes to induce fractures [8]. Three different cases were considered:

- Case 1:* $Q_0 = 0.08m^3/s$ at $t = 7200s$,
- Case 2:* $Q_0 = 0.04m^3/s$ at $t = 14400s$,
- Case 3:* $Q_0 = 0.16m^3/s$ at $t = 3600s$.

Three different time instants have been chosen for each flow rate so that the product $Q_0 \frac{\rho_0}{\rho} t$, where ρ_0 is the density of the fluid when the depth is null, ρ is the density that varies with the depth and t is the time, remains constant.

Figure 5.9 show exactly what the theory suggests: even if the mass remains constant, it has a big influence on the fracture radius. The injection flow rate does not interests the Carter’s leak off directly, but the results match with the theory according to which the lower the flow, the more infiltration will be.

5.3.2 Toughness

When the leak-off is negligible, the higher the fracture toughness of the rock, the smaller the fractures at any given time [17]. In this case, it is evident that it is not possible to approximate the leak-off as negligible, but as seen in Equation 5.1, it influences the Carter’s leak-off just because the Δp depends directly on the toughness (Equation 4.5).

Two different trend of the K_I are considered in Figure 5.10:

- Case 1:* K_I follows temperature-dependent values of the toughness, as in Figure 5.2c,
- Case 2:* K_I is defined as a constant values of toughness at ambient temperature.

The difference between the toughness in *Case 1* and *Case 2* is negligible and, since the influence on the C_L is very low, the predicted fracture radius in both cases and in both wellbores does not change significantly (Figure 5.11).

It is possible to state that the influence of the temperature-dependent toughness on the radius is very low. For this case, it would be safe to assume constant toughness.

5.3.3 Carter's leak-off

It is evident from Equation 5.1 that the Carter's leak-off, the square of compressibility, of permeability and of porosity are directly proportional; these three fluid's parameters have been changed to study first of all the influence that they have on the leak-off and secondly how the increase and the decrease of the C_L affects the fracture radius. The three other cases considered in this section are:

Case 1: $k(d, t)$, $\varphi(d, t)$ and $c_t(d, t)$ follow their real trends, as in Figure 5.2b and in Tables ?? and ??;

Case 2: $c_t = 4.43 \cdot 10^{-10} Pa$, $k(d, t)$ and $\varphi(d, t)$ follow their real trends as in Tables ?? and ??;

Case 3: $k = k(d, t) \cdot 10^{-2} Pa$, $c_t(d, t)$ and $\varphi(d, t)$ follow their real trends as in Figure 5.2b and in Tables ?? and ??, respectively;

Case 4: $\varphi = 1 \cdot 10^{-2} Pa$, $c_t(d, t)$ and $k(d, t)$ follow their real trends as in Figure 5.2b and in Tables ?? and ??, respectively.

As said before, what is expected is that if one of these three parameters increase, the C_L also increases (Figure 5.12), and this means that the fracture radius should decrease, which is in line with the results obtained, shown in Figure 5.13.

5.3.4 Viscosity

The fluid dissipation becomes increases with the fluid viscosity; instead when a low-viscosity flow is used, the fluid infiltrates into the medium easily.

In Figure 5.14, the real case (*Case 1*) is compared with another one where the viscosity is constant and set equal to $8 \cdot 10^{-4}$ (*Case 2*).

As expected, when the viscosity increases, the fracture radius increases because of the lower leak-off. Furthermore it is demonstrated in Appendix A that high viscosity fracturing fluid results in local fluid-loss velocity.

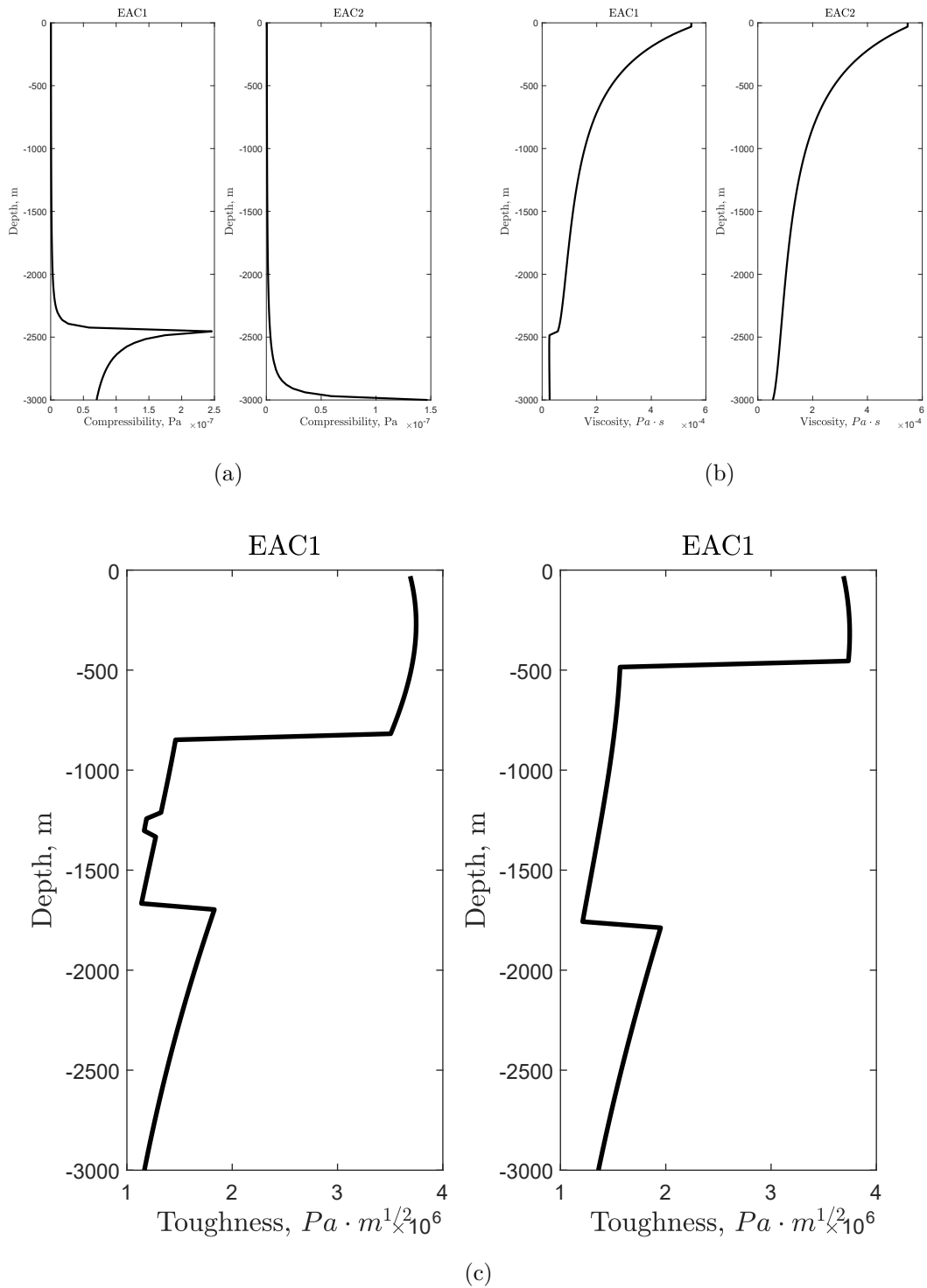


Figure 5.2: Compressibility, viscosity and toughness trend as a function of the depth for both wellbore EAC1 and EAC2.

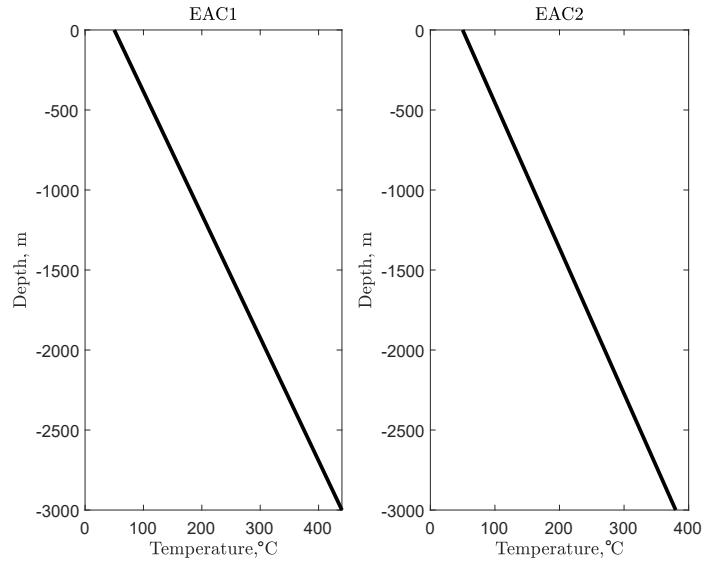


Figure 5.3: Temperature trend as a function of the depth for both wellbore EAC1 and EAC2.

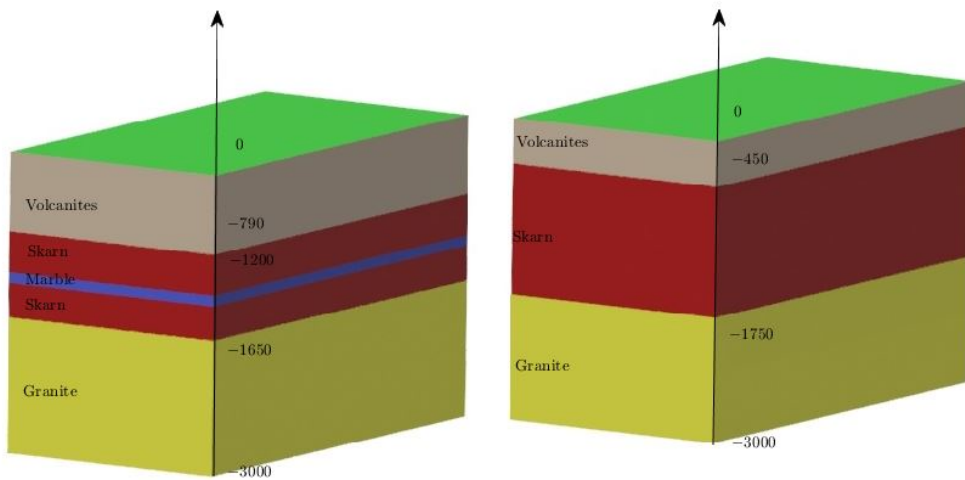


Figure 5.4: The main cross-section for EAC1 and EAC2 wellbores.

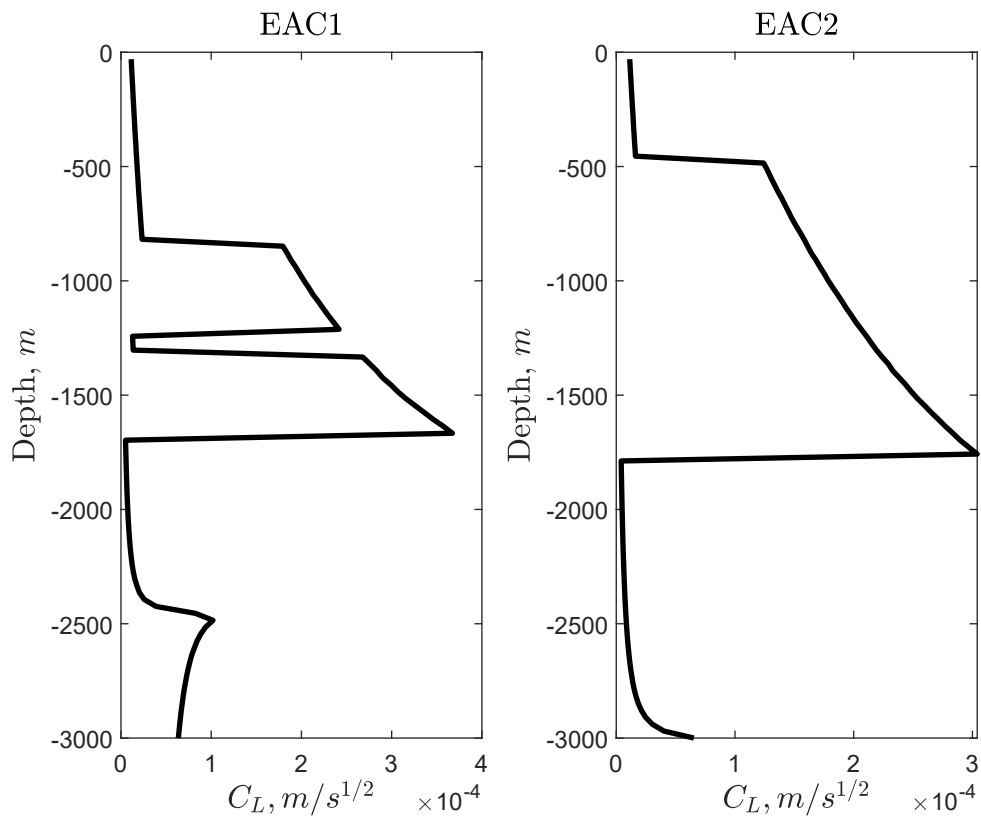


Figure 5.5: Carter's leak-off trend as a function of the depth for both wellbore EAC1 and EAC2.

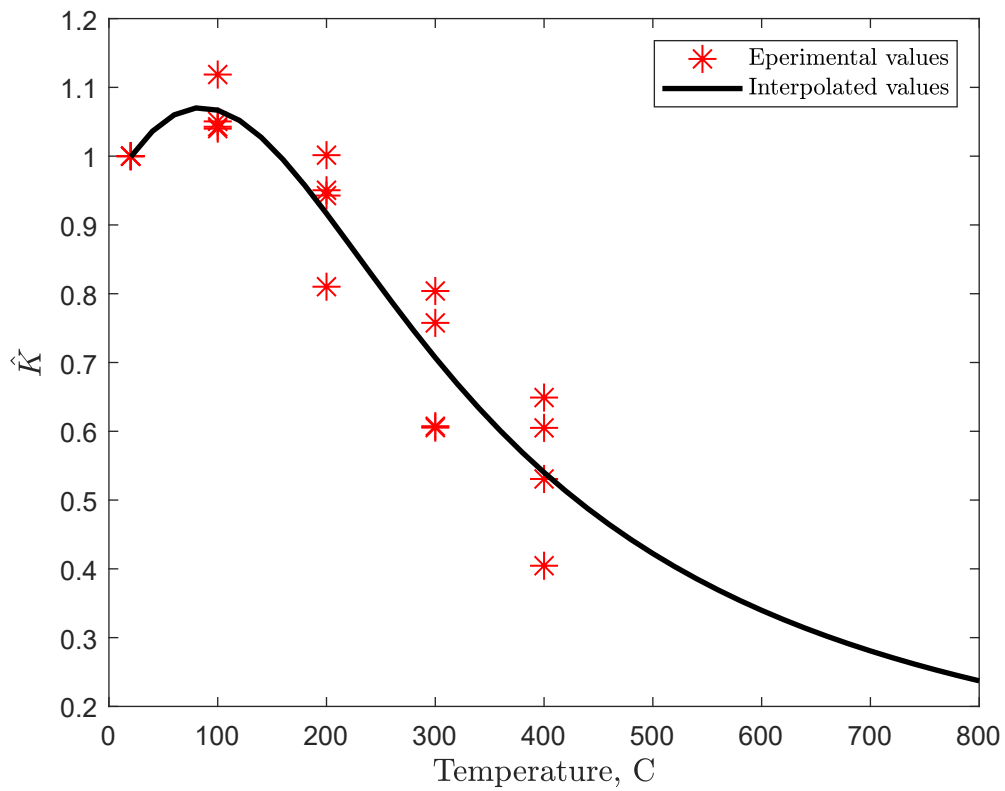


Figure 5.6: \hat{K} trend as a function of the temperature.

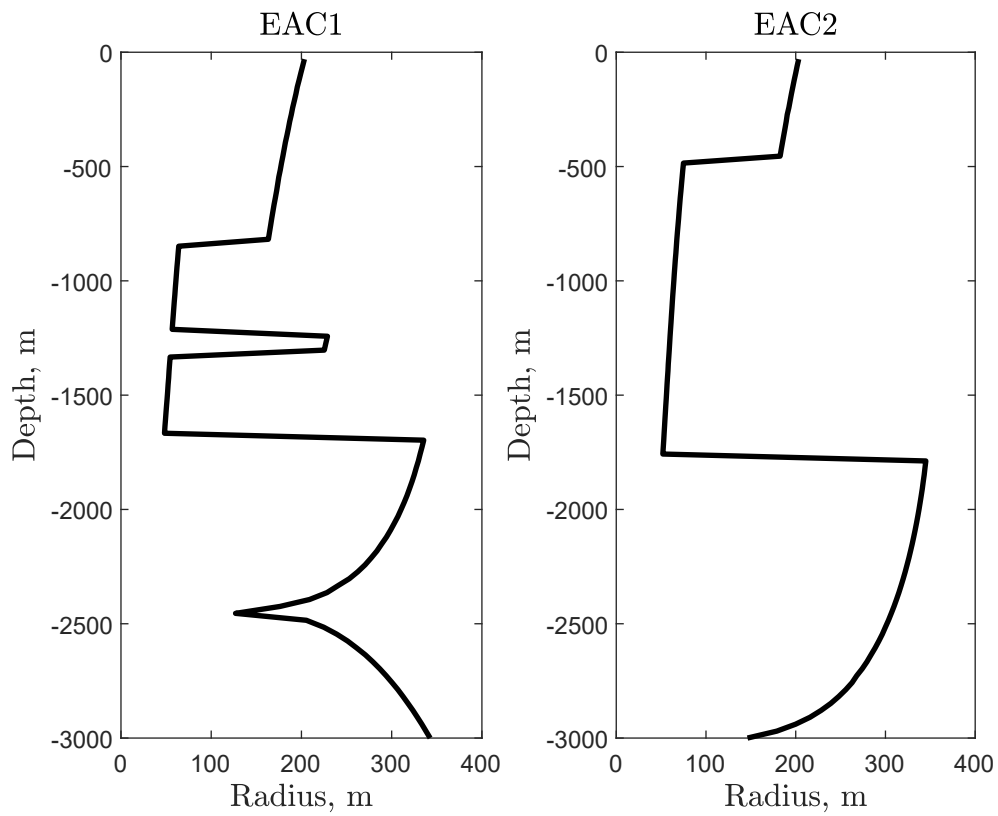


Figure 5.7: Fracture radius trend as a function of the depth for both wellbore EAC1 and EAC2 at time $t = 7200s$.

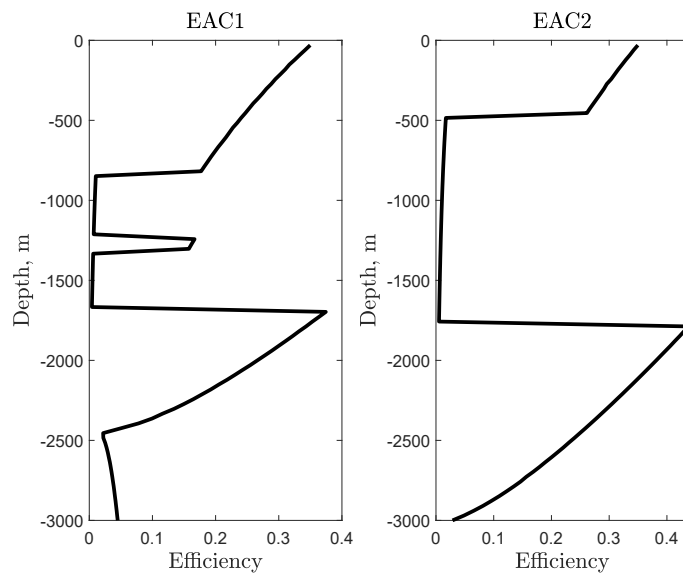


Figure 5.8: Efficiency trend as a function of the depth for both wellbore EAC1 and EAC2 at time $t = 7200s$.

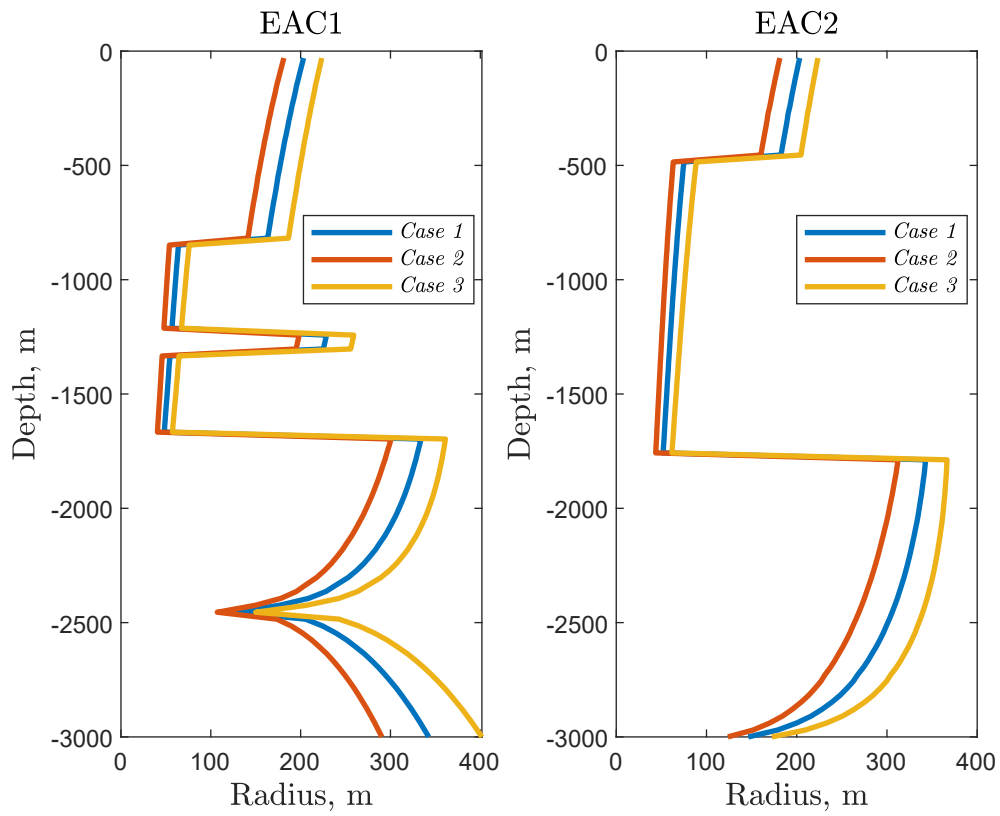


Figure 5.9: Fracture radius trend for both wellbore EAC1 and EAC2 at different instant times and different flow rate. Blue line - $Q_0 = 0.08m^3/s$ at $t = 7200s$, red line - $Q_0 = 0.04m^3/s$ at $t = 14400s$, yellow line - $Q_0 = 0.16m^3/s$ at $t = 3600s$.

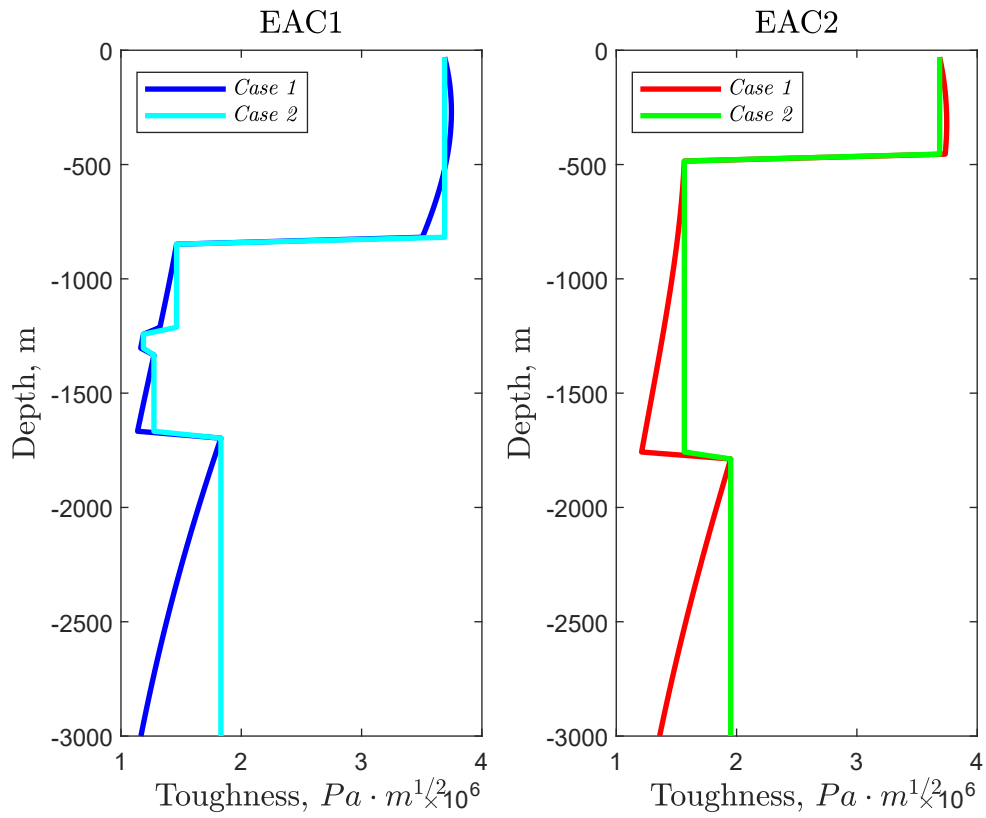


Figure 5.10: K_I as a function of the depth in the two different considered cases for both wellbore EAC1 and EAC2.

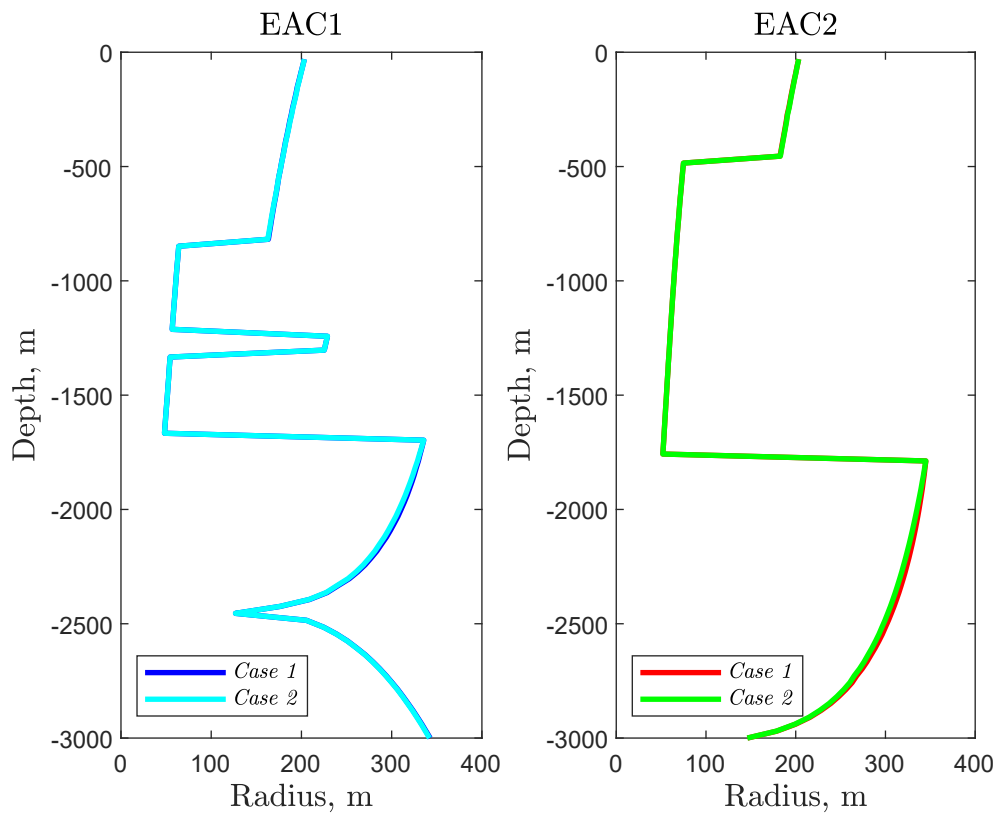


Figure 5.11: Fracture radius trend as a function of the depth for both wellbore EAC1 and EAC2 at different time $t = 7200s$.

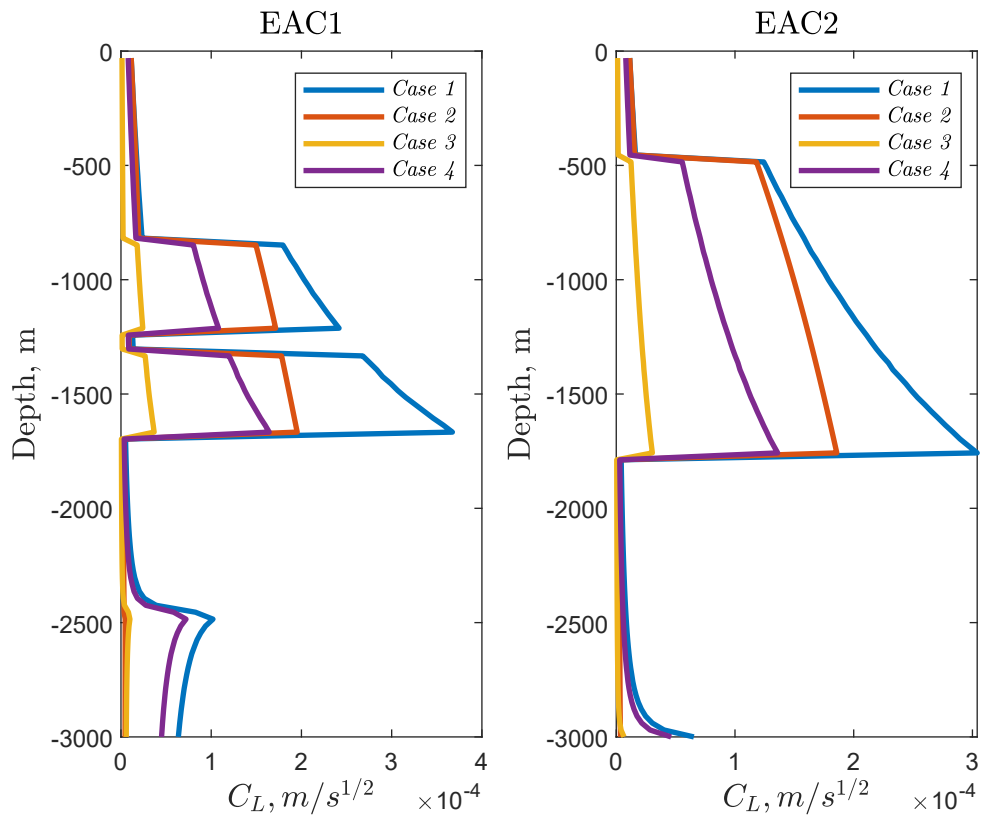


Figure 5.12: Carter's leak-off coefficient trend for both wellbore EAC1 and EAC2 with different flow rate. Blue line - $Q_0 = 0.08m^3/s$, red line - $Q_0 = 0.04m^3/s$, yellow line - $Q_0 = 0.16m^3/s$.

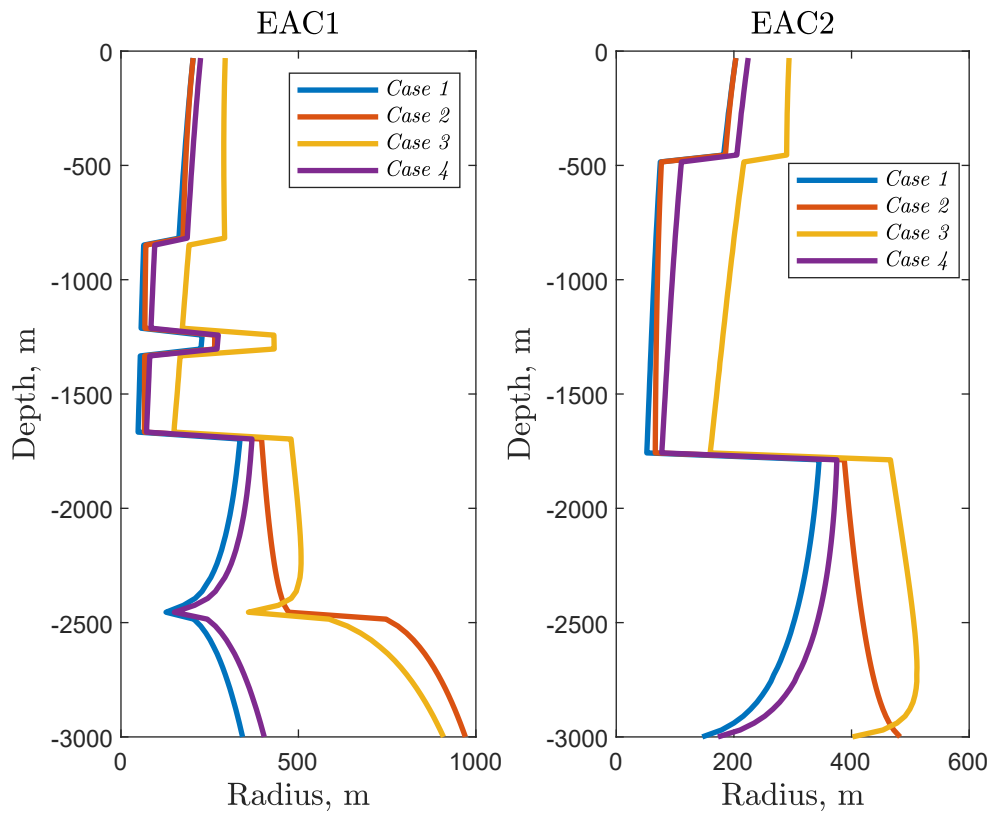


Figure 5.13: Fracture radius trend for both wellbore EAC1 and EAC2 at different instant times and different flow rate. Blue line - $Q_0 = 0.08m^3/s$ at $t = 7200s$, red line - $Q_0 = 0.04m^3/s$ at $t = 14400s$, yellow line - $Q_0 = 0.16m^3/s$ at $t = 3600s$.

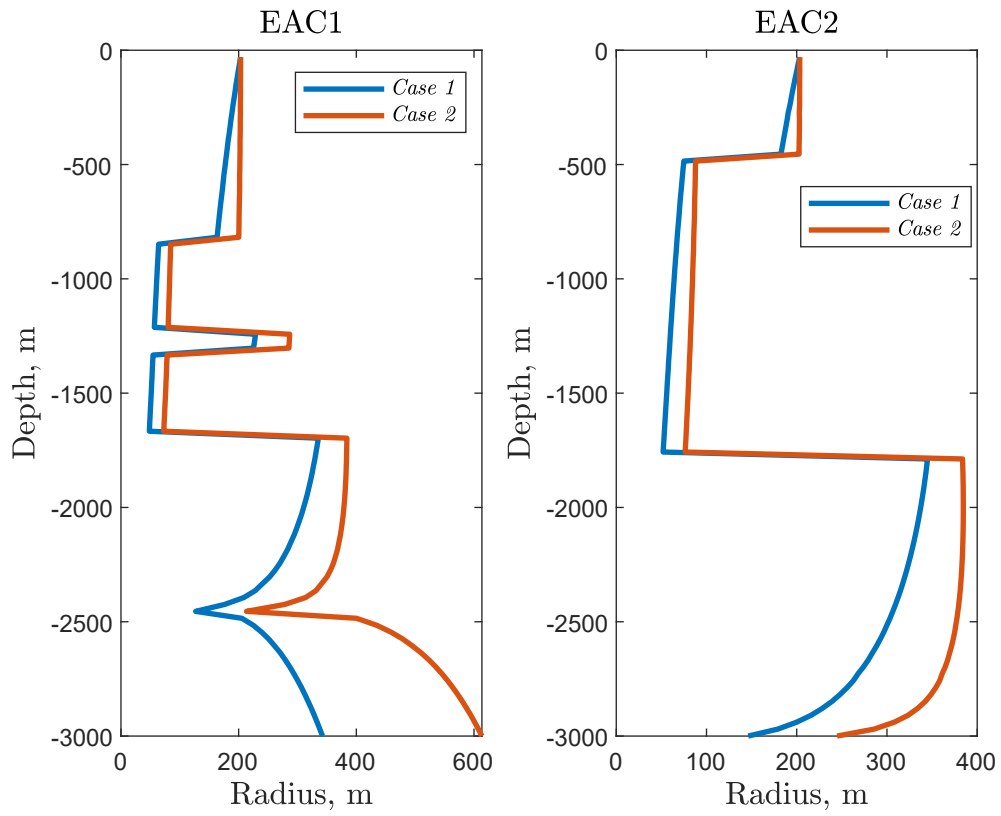


Figure 5.14: Viscosity trend for both wellbore EAC1 and EAC2 at different instant times and different flow rate.

Chapter 6

Conclusions

The first objective of this research is to analyze the propagation regimes of a penny-shaped hydraulic fracture; the asymptotic solutions have been constructed because they constitute benchmarks which have been used by Dontsov to validate his numerical algorithm, regarding the fracture radius, the fluid pressure and the fracture width. This allows to apply this method to simulate what should be the most realistic behavior of the hydraulic fracturing in the two specific wells: EAC1 and EAC2.

After having analyzed what is the influence of the rock and of the fluid's parameters on the fracture radius and on the efficiency, it is important to focus on the optimal depth.

The probable optimal depth of simulation is found considering the efficiency's value and the fracture radius' value, as well.

The results that show the depth in which the fracture radius is bigger (Figure 5.7), are summarized in Table 6.1 are commented below:

- in EAC1, fracture radius value reaches the maximum value at the end of the considered depth;
- in EAC2, the maximum radius' value is reached not at the lower depth that means at the higher reached temperature, so as it happens in the EAC1 well-bore.

Concerning the efficiency, from Figure 5.8, the results obtained in the same conditions are summarized in Table 6.2.

In the EAC1 is clear that the efficiency is very low compared to the EAC2 well's efficiency. However, from the Figure 5.7 it is possible to locate the second bigger fracture radius (335 m) at -16970 m, where the efficiency is 40%; this means that even if the fracture radius is lower than the other one at -3000 m of the 2%, the efficiency turns out to be higher that the efficiency at the lower depth of ten times.

	EAC1	EAC2
Depth, m	–3000	–1787.9
Fracture Radius, m	342.69	345

Table 6.1: Maximum values of the fracture radius and the corresponding depth for both wellbore EAC1 and EAC2.

	EAC1	EAC2
Depth, m	–3000	–1787.9
Efficiency	4%	40%

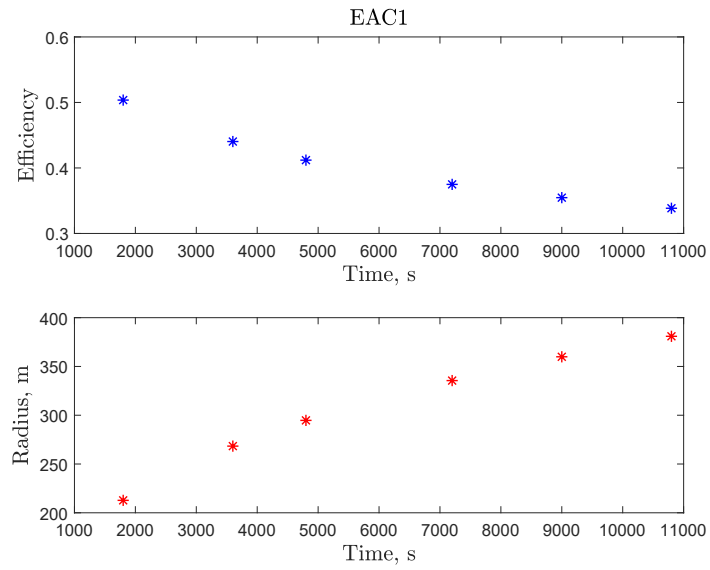
Table 6.2: Efficiency’s values at the depths where the fracture radius is maximum for both wellbores EAC1 and EAC2.

The best depth where it is possible to obtain the maximum efficiency is in correspondence of the depth where the fracture radius is also the maximum; indeed it is important to consider the cost to dig deeper wells.

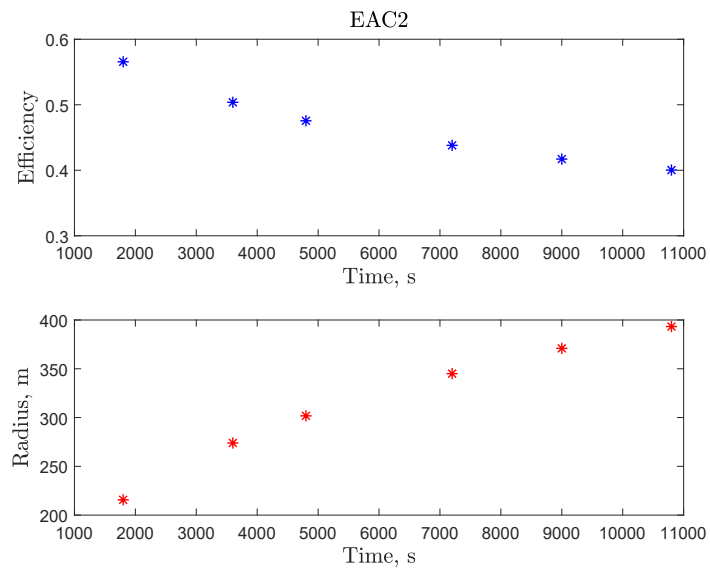
The evolution of the fracture radius and of the efficiency over the time at –1697 m and –1787.9 m, for both wells EAC1 and EAC2, are shown in Figure 6.1a and 6.1b respectively.

As expected, the fracture radius increases and the efficiency decreases and the higher is the time, the lower is the velocity with which the radius and the efficiency increases and decreases, respectively.

Using again the map introduced in Figure 4.1, it is simple to see the way followed by evolution parameter over the time; considering the evolution in a point of the depth that corresponds to –1697 m and –1787.9 m for EAC1 and EAC2, respectively, means having one constant value of the ϕ per well as a function of the time, so the path of the system follows a straight line. The evolution of the global solution for both cases is driven entirely by the simultaneous decrease of the tip velocity and increase of the crack length as time proceeds. These two combined effects cause a progressive shift of the main source of energy dissipation from viscous flow at small time to fracture energy at large time. This transition is effected by a



(a)



(b)

Figure 6.1: Fracture radius and efficiency trend over the time for both wellbores EAC1 and EAC2.

change of the dominant asymptote at the fracture scale, from M -vertex solution at small time to K - asymptote at large time [4].

It is interesting to compare the efficiency trend over the time when the depth

is -3000 m, Figure 6.2.

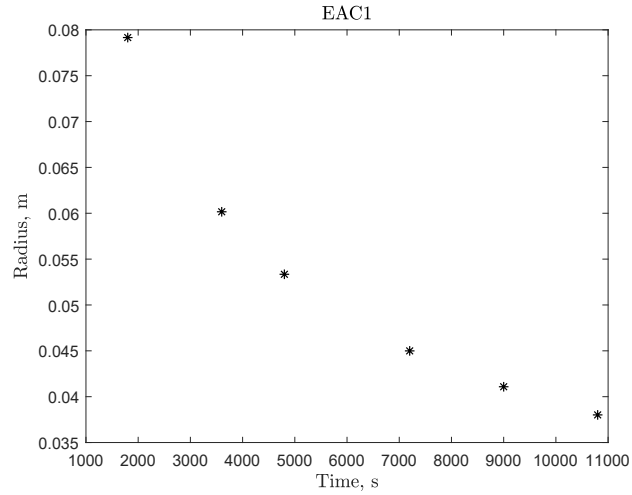


Figure 6.2: Efficiency trend over the time for both wellbores EAC1 at 3000 m depth.

The efficiency trend at 3000 m depth is smaller than $495 \div 711\%$ compared to the efficiency trend at 1697 m (Figure ??). This conclusion confirms what said before: the optimal depth to be excavated is not in the deepest point of the well, but it is about 1300 m above.

Appendix A

Carter's leak off

The carter leak-off coefficient includes three effects that may act simultaneously [10]:

1. viscosity and relative permeability effect of fracturing fluid;
2. reservoir-fluid viscosity-compressibility effects;
3. wall-building effects.

The fluid in the porous medium is treated as $1D$ model based on the following equation [9]

$$\frac{\partial p}{\partial t} = K \frac{\partial^2 p}{\partial x^2}, \quad x > 0, t > 0, \quad (\text{A.1})$$

where K is the conductivity defined as

$$K = \frac{k_0}{\mu \rho_0 c_i}, \quad (\text{A.2})$$

and where k_0 and ρ_0 are constant permeability and density at the reference state. Initial and boundary conditions are expressed by 5.3 and, applying them to the A.1, the analytical solution is obtained:

$$p(x, t) = (p_c - p_0) \operatorname{erfc} \left(\frac{x}{2\sqrt{Kt}} \right) + p_0, \quad (\text{A.3})$$

where

$$\operatorname{erfc}(z) = 1 - \operatorname{erf}(z), \quad \operatorname{erf}(z) = \frac{2}{\sqrt{\pi}} \int_0^z e^{-\eta^2} d\eta. \quad (\text{A.4})$$

The function $\operatorname{erf}(z)$ is known as error function and these conditions are valid:

- $\operatorname{erf}(0) = 0$
- $\operatorname{erf}(\infty) = 1$

From the analytical solution, it is possible to obtain the leak-off velocity with this procedure

$$\begin{aligned}\frac{\partial p}{\partial x} &= -\Delta p \frac{2}{\sqrt{\pi}} \frac{\partial}{\partial x} \int_0^{\frac{x}{2\sqrt{Kt}}} e^{-\lambda^2} d\lambda \\ &= -\Delta p \frac{2}{\sqrt{\pi}} e^{-x^2} \frac{1}{2\sqrt{Kt}}.\end{aligned}\tag{A.5}$$

Introducing now the Darcy law in tensor form,

$$v_i = \frac{1}{\mu} (k_{ij} p_{,j}), \quad p_{,j} = \frac{\partial p}{\partial x_j}\tag{A.6}$$

where i, j are the coordinate components x, y and z ;
knowing the Einstein summation convention that implies what follows

$$k_{ij} * \frac{\partial p}{\partial x_j} = k_{i1} * \frac{\partial p}{\partial x_1} + k_{i2} \frac{\partial p}{\partial x_2} + k_{i3} * \frac{\partial p}{\partial x_3}.\tag{A.7}$$

Substituting Equation A.5 into Equation A.6, for 1D fluid in homogeneous and isotropic porous medium, the fluid velocity is

$$\begin{aligned}v &= -\frac{k}{f} 6.1 \frac{\partial p}{\partial x} \\ &= \frac{k e^{-x^2} \Delta p}{\mu \sqrt{\pi Kt}}.\end{aligned}\tag{A.8}$$

Finally, the leak-off velocity in hydraulic fracturing is defined as the fluid velocity when the x coordinate is null, i.e.

$$v_L = \frac{k}{\mu} \frac{\Delta p}{\sqrt{\pi Kt}}.\tag{A.9}$$

The v_L term measures how fast the fluid inside a fracture leaks to the surrounding porous medium.

Here the Carter’s leak-off coefficient is defined as

$$C_L = \frac{k \Delta p}{\mu \sqrt{\pi K}},\tag{A.10}$$

and, using the Equation A.2, so as

$$C_L = \Delta p \sqrt{\frac{k \varphi c_t}{\mu \pi}}.\tag{A.11}$$

Bibliography

- [1] M.J. Bouteica et al. “Hydraulic Fracturing Model Based on a 3D Closed Form: Tests, Analysis of Fracture Geometry, and Containment”. In: *Low Permeability Reservoirs Symposium*. Society of Petroleum Engineers. 1987.
- [2] Philippe Calcagno et al. “Preliminary 3-D geological models of Los Humeros and Aocolco geothermal fields (Mexico)–H2020 GEMex Project”. In: *Advances in Geosciences* 45 (2018), pp. 321–333.
- [3] M. P. Cleary and S. K. Wong. “Numerical simulation of unsteady fluid flow and propagation of a circular hydraulic fracture”. In: *International Journal for Numerical and Analytical Methods in Geomechanics* 9.1 (1985), pp. 1–14.
- [4] E. Detournay. “Mechanics of hydraulic fractures”. In: *Annual Review of Fluid Mechanics* 48 (2016), pp. 311–339.
- [5] E.V. Dontsov. “An approximate solution for a penny-shaped hydraulic fracture that accounts for fracture toughness, fluid viscosity and leak-off”. In: *Royal Society open science* 3.12 (2016), p. 160737.
- [6] E.V. Dontsov and A.P. Peirce. “A multiscale implicit level set algorithm (ILSA) to model hydraulic fracture propagation incorporating combined viscous, toughness, and leak-off asymptotics”. In: *Computer Methods in Applied Mechanics and Engineering* 313 (2017), pp. 53–84.
- [7] E.V. Dontsov, A.P. Peirce, et al. “Implementing a universal tip asymptotic solution into an implicit level set algorithm (ILSA) for multiple parallel hydraulic fractures”. In: *50th US Rock Mechanics/Geomechanics Symposium*. American Rock Mechanics Association. 2016.
- [8] Kang Duan et al. “DEM modeling of hydraulic fracturing in permeable rock: influence of viscosity, injection rate and in situ states”. In: *Acta Geotechnica* (), pp. 1–16.
- [9] *Fluid flow in porous media and Carter’s equation*. <http://www.frackoptima.com/userguide/theory/fluidflow-porousmedium-carter.html>.
- [10] Tsuyoshi Ishida et al. “Influence of fluid viscosity on the hydraulic fracturing mechanism”. In: *Journal of energy resources technology* 126.3 (2004), pp. 190–200.

BIBLIOGRAPHY

- [11] M.V. Madyarova. *Fluid-driven Penny-shaped Fracture in Elastic Medium*. University of Minnesota, 2003.
- [12] PG Meredith and BK Atkinson. “Fracture toughness and subcritical crack growth during high-temperature tensile deformation of Westerly granite and Black gabbro”. In: *Physics of the Earth and Planetary Interiors* 39.1 (1985), pp. 33–51.
- [13] L. Peiffer, C. Wanner, and L. Pan. “Numerical modeling of cold magmatic CO₂ flux measurements for the exploration of hidden geothermal systems”. In: *Journal of Geophysical Research: Solid Earth* 120.10 (2015), pp. 6856–6877.
- [14] A.P. Peirce and E. Detournay. “An implicit level set method for modeling hydraulically driven fractures”. In: *Computer Methods in Applied Mechanics and Engineering* 197.33-40 (2008), pp. 2858–2885.
- [15] C.L. Pulido, M.F. Armenta, and G.R. Silva. “Characterization of the Acoculco geothermal zone as a HDR system”. In: *Transactions - Geothermal Resources Council* 34 (Jan. 2010), pp. 337–340.
- [16] A.A. Savitski and E. Detournay. “Propagation of a penny-shaped fluid-driven fracture in an impermeable rock: asymptotic solutions”. In: *International Journal of Solids and Structures* 39.26 (2002), pp. 6311–6337.
- [17] M Thiercelin, RG Jeffrey, K Ben Naceur, et al. “The Influence of Fracture Toughness on the Geometry of Hydraulic Fractures”. In: *Low Permeability Reservoirs Symposium*. Society of Petroleum Engineers. 1987.
- [18] P. Valko and Michael J. E. *Hydraulic fracture mechanics*. Vol. 28. Wiley New York, 1995.